©2017 Uspekhi Fizicheskikh Nauk, Russian Academy of Sciences

REVIEWS OF TOPICAL PROBLEMS

PACS numbers: 71.18.+y, 73.20.–r, 73.25.+i, 73.43.–f

Quantum oscillations in three-dimensional topological insulators

S I Vedeneev

DOI: https://doi.org/10.3367/UFNe.2017.01.038053

Contents

Abstract. **The basic concepts behind topological insulators are briefly reviewed. After discussing what makes some insulators topological and giving a brief history of this rapidly growing field, recent successes in experiments with these exotic materials are discussed.**

Keywords: topological insulator, Dirac fermions, surface state, quantum oscillations

1. Introduction

During the last several years, a new class of quantum materials in the field of condensed matter physics has appeared — three-dimensional (3D) topological insulators, which have attracted the attention of many scientists (see, e.g., reviews [1, 2]). Topology studies those properties of objects that are invariant under transformations. The term 'topological invariance' was introduced by mathematicians in order to classify different geometrical objects within broad classes. In mathematics, topological classification does not describe small details and is focused on fundamental differences between shapes. A classical example is the transformation of a sphere into an ellipsoid. The surface of a perfect sphere is topologically equivalent to the surface of an ellipsoid because these surfaces can be transformed into each other without creating any holes, just by compressing or stretching along one of the axes.

In its simplest description, the topological insulator (TI) is an insulator that always has a metal surface when it is in contact with a vacuum or a conventional insulator (dielectric). Metal states occur when the surface 'disentangles' the wave functions of entangled electrons. Moore suggested an intuitive example of a TI [3], a trefoil knot (Fig. 1a) and a ring (Fig. 1b), which he respectively called topological and conventional insulators. Due to the topological nonequivalence of their geometrical shapes, these objects cannot be continuously ('adiabatically') transformed into each other without making any cuts [3].

In many-particle systems with a band gap separating the ground state from excited states, an adiabatic deformation can be defined as a change that does not close the gap. This topological concept can be applied to both insulators and superconductors with a bang gap, but it cannot be applied to gapless states inherent to metals and doped semiconductors. According to this general definition, a state with a gap cannot be transformed into a state with a gap belonging to another topological class unless a quantum phase transition occurs, after which the system becomes gapless. This simple argument shows that such an abstract concept as topological classification can be applied to solid-state systems with an energy gap [4].

It is known that atoms and electrons can form different states of matter, which can be classified by their symmetries (translational, rotational, etc.), according to the principle of spontaneous symmetry breaking. For example, a magnetic field breaks the rotational symmetry in a crystal, despite the isotropy of fundamental interactions, and gauge symmetry is broken in superconductors, which leads to such phenomena as flux quantization and Josephson effects [1]. In 1980, a new state with the quantum Hall effect [5] was added to these states. This was the first example of a quantum state that does not exhibit spontaneous symmetry breaking. The evolution of such a state depends only on its topology, not on its specific geometry. This state is topologically different from any other previously known state of matter.

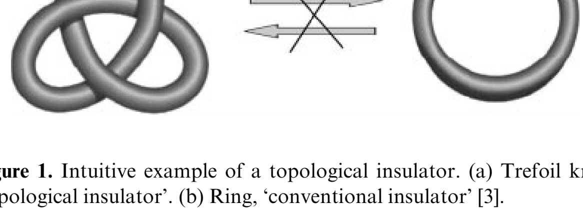

Figure 1. Intuitive example of a topological insulator. (a) Trefoil knot, 'topological insulator'. (b) Ring, 'conventional insulator' [3].

S I Vedeneev Lebedev Physical Institute, Russian Academy of Sciences, Leninskii prosp. 53, 119991 Moscow, Russian Federation
E-mail: vedeneev@sci.lebedev.ru

Received 22 December 2015, revised 25 May 2016
Uspekhi Fizicheskikh Nauk **187** (4) 411 – 429 (2017)
DOI: https://doi.org/10.3367/UFNr.2017.01.038053
Translated by A L Chekhov; edited by A M Semikhatov

1.1 Quantum Hall effect

The quantum Hall effect or the quantization of the Hall (transverse) conductivity in two-dimensional (2D) semiconductors was discovered more than 35 years ago and was a great surprise (for this discovery, Klaus von Klitzing received a Nobel Prize in 1985). This effect is observed in strong magnetic fields at low temperatures and corresponds to the fact that in 2D electron layers, the dependence of the transverse resistance ρ_{xy} on the magnitude of the magnetic field normal to the surface (or on the carrier concentration in a fixed magnetic field) is not smooth. This dependence is made of steps or 'plateaus' with constant transverse resistance (Fig. 2a). The ρ_{xy} values at the steps can be expressed through fundamental constants: $\rho_{xy} = h/Ne^2$, where e is the electron charge, h is the Planck constant, and N is an integer. Such a quantized transport term clearly indicates a macroscopic quantum phenomenon.

The Lorentz force acts on electrons moving in the magnetic field and drives their rotation at the cyclotron frequency ω_c. According to laws of quantum mechanics, the particles that move periodically can have only discrete energy levels. Hence, the electron spectrum in a magnetic field consists of Landau levels with the energies $E_N = \hbar\omega_c(N+1/2)$, where $\hbar = h/(2\pi)$. If N Landau levels are filled and the others are empty, the filled and empty states are separated by an energy gap similar to the band gap in an insulator. A depleting electric field forms near the edges of a 2D sample in the magnetic field and 'lifts up' the Landau levels [7]. In crossed magnetic and electric fields, an electron drifts along equipotential lines. Edge current states form near the structure edges, which leads to the Hall current with a quantized Hall conductivity $\sigma_{xy} = Ne^2/h$ [8]. Steps with a constant transverse resistance ρ_{xy} are observed when the chemical potential is located between two Landau levels, as takes place in insulators. (For the degenerate electron gas at zero temperature, the chemical potential coincides with the Fermi energy.)

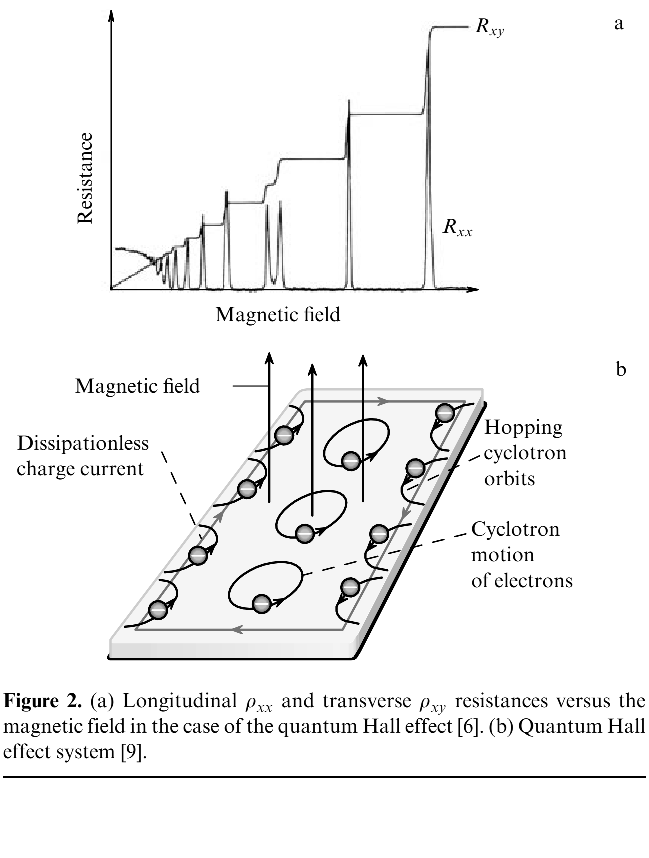

Figure 2. (a) Longitudinal ρ_{xx} and transverse ρ_{xy} resistances versus the magnetic field in the case of the quantum Hall effect [6]. (b) Quantum Hall effect system [9].

At the same time, the longitudinal resistance ρ_{xx} (the ratio of the voltage drop along the current direction to the magnitude of this current) vanishes (Fig. 2a) and a dissipationless charge current flows through the structure. Zero damping is explained by the fact that for damping to occur, the electrons must make a transition to the higher Landau levels and overcome the energy intervals.

In the state responsible for the quantum Hall effect, the larger part of the 2D sample is an insulator and the charge current flows along the edges only through 1D conducting channels. The current in each of these channels flows in one direction, which is defined by the sign of the quantizing magnetic field. Because the edge states have no backscattering, the current in edge channels is dissipationless. This surface state can be described by the motion of electrons along cyclotron orbits, while bouncing from the edges of the sample (Fig. 2b) [9]. The number of edge channels in the sample is directly connected with the value of the quantized conductance σ_{xy} [10]. (We do not discuss the fractional quantum Hall effect here.) This state defines a topological phase such that the fundamental property of Hall conductance is topologically protected, which means that it remains constant despite small changes in the sample and cannot be altered until the system experiences a quantum phase transition [8]. Detailed information about the quantum Hall effect can be found, e.g., in [11, 12].

A system in a quantum Hall state can be considered a TI, which is the first example of a quantum state that is topologically different from all states of matter known before the discovery of the quantum Hall effect. (In reality, the term 'topological insulator' was first introduced in [13], where it was assumed that a TI can exist among 3D systems.) A state with the quantum Hall effect belongs to the topological class that simultaneously has to be two-dimensional and break the time-reversal symmetry (T symmetry) by the presence, for example, of a magnetic field. (Equations of classical mechanics, classical electrodynamics, quantum electrodynamics, and the theory of relativity are unchanged under time reversal. In the microworld, T symmetry is violated by weak interactions.)

A simple example of a quantum Hall effect in band theory is the model of graphene (2D structure of carbon) in a magnetic field, introduced by Haldane [14]. Figure 3 shows the electron spectrum of a 2D sample in the quantum Hall state according to the Haldane model. Valence and conduction bands are separated by a band gap and are connected through a topologically protected 1D edge state, which is characterized by the Dirac linear dispersion $E = \pm v_F p$, where v_F is the electron Fermi velocity and p is its momentum.

To summarize, a 2D insulator in a quantum Hall state has a band gap in the bulk and a topologically protected gapless edge state. The existence of gapless conducting states near the interface (for example, between the structure with the quantum Hall effect and a vacuum) where the topological invariance changes is the main result of the topological classification [7]. More detailed information on edge states can be found, e.g., in [15].

1.2 Quantum spin Hall effect. Two-dimensional topological insulators

Twenty-six years after the discovery of the quantum Hall effect, it was predicted theoretically in [16] that there is a possibility of a spin-current state in 2D systems in an electric field similar to the quantum Hall state but without a

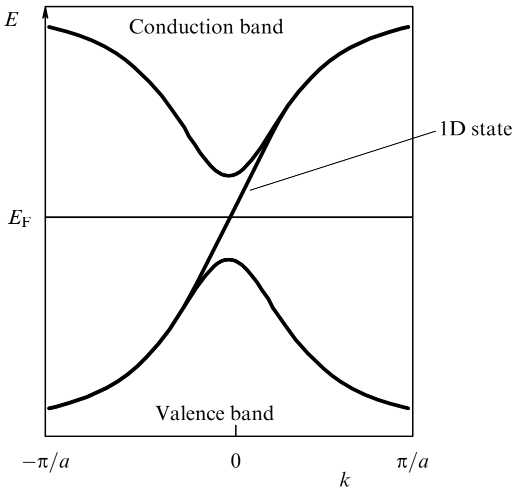

Figure 3. Electron spectrum of a 2D structure versus the momentum along the edges in the Haldane model [14]. Valence and conduction bands in the major part of the 2D sample are separated by a band gap and are connected through a one-dimensional state with linear dispersion [8].

macroscopic magnetic field. (Spin current is the spin flow not accompanied by charge transfer. Usually, the electric current does not carry spin, because electron spins are oriented randomly.) We note that spin currents have been of great interest in solid state physics for a long time already, because they open up possibilities of spin electronics (spintronics) [17]. Since 1970, scientists have started to discuss the possibility of observing the spin Hall effect by applying an external electric field, which should deflect the charge carriers with opposite spins in opposite directions perpendicular to the electric field (see, e.g., [18]). A major success in this field was achieved in [19]. The authors assumed that the connection between physics and topology in insulators could be more fundamental than in the case of a simple quantum Hall effect state. In searching for a new topological class, the authors of [19] have shown that some pure and doped semiconductors (for example, Si, Ge, InSb, and GaAs or GaAs heterostructures) can demonstrate the spin Hall effect due to the time reversal symmetry and spin–orbit coupling similar to the way this occurs in graphene, where the band gap is formed due to the spin–orbit coupling. At the same time, questions remained regarding the effects associated with disorder. It was assumed that the spin current, just as in the case of the quantum Hall effect, would be dissipationless. However, in this case, even if the spin current does not lead to Joule heating, the external electric field induces a charge current with losses due to the nonzero sample resistance.

In a subsequent study [20], the same authors theoretically predicted the possibility of observing the dissipationless spin Hall effect without any charge current in 3D band insulators HgTe and HgSe. This effect is similar to the quantum Hall effect, but the spin Hall conductivity is not quantized even in 2D systems and depends on the parameters characterizing the band structure. In the considered case, the electrons can move in an external electric field, but the direction of their motion must depend on the spin direction due to the anisotropy of electron scattering on impurities. Such spin currents in filled bands do not suppress each other and Hall spin conductivity can exist even in a band insulator. As in [19], the spin–orbit coupling was responsible for the spin conductivity. This was the first example of a nontrivial topological structure in a band insulator without a magnetic field. The authors of [14, 19–22] developed an important concept of an insulator that was afterwards called the quantum spin Hall insulator or the two-dimensional topological insulator (2D TI). The most important result of these papers was that the suggested models did not require violation of time reversal symmetry.

Extrinsic and intrinsic spin effects can be distinguished. In the first case, which was theoretically predicted in [18], the main factor is nonsymmetric spin-dependent scattering on the impurity potential, while the second case depends on the interaction of electron spin and orbital motion in the periodic lattice of the material. In both cases, the spin–orbit coupling characterizes the process in which a simultaneous change in the electron spin and orbital momentum takes place. Entanglement of spin and orbital momentum is a relativistic effect, which can be derived from the Dirac equation for the electron [23].

A key improvement in the 2D TI theory was made in [24, 25], where a new type of topological invariance was proposed that can be present in a conventional insulator. In studying the quantum spin Hall effect in graphene, which was discovered at that time, the authors suggested a specific 2D TI model and showed that a finite spin–orbit coupling in graphene leads to the formation of a band gap.

This means that a state with the quantum spin Hall effect, or a 2D TI, has an energy gap in the bulk and two gapless spin-selective edge states on the sample boundaries [26]. One of the characteristic properties of massless Dirac fermions is associated with the Berry phase, due to which back-scattering is absent in the material. We note that the linear dispersion law of graphene leads to a linear dependence of the density of states on energy [16, 17], in contrast to the conventional parabolic dispersion law $E = p^2/2m^*$ (where m^* is the effective mass) in ordinary 2D systems. Such an analogy with graphene is used because it can help to better describe 2D TIs and because the Dirac electron physics in graphene is similar to that on the surface of a 3D TI with only one difference: the numbers of Dirac cones in these two cases are not the same.

The authors of [24, 25] also showed that despite the instability of electron edge states in previous models (in particular, due to impurities), there are real 2D materials that must have stable edge states in the absence of a magnetic field. Their model, as in the case of graphene, is based on the relativistic effect of spin–orbit coupling, in which the electron spin and orbital momentum degrees of freedom are coupled and, due to this coupling, moving electrons ‘feel’ a spin-dependent force even in nonmagnetic materials. Such electron motion is coherent and leads to a collective state, which is stable because the energy needed to destroy it equals the band gap. This results in the formation of one-dimensional current ‘loops’ at the sample edges with spin up and spin down flowing in opposite directions, as is schematically shown in Fig. 4a. The state with the quantum spin Hall effect can be roughly represented as two copies of spatially separated states with the quantum Hall effect, distinguished only by different spin directions. The currents in a sample with such states flow along the edges in opposite directions. Because each current is unidirectional, back-scattering is not possible, and a dissipationless spin current with no charge current must form in the structure.

Figure 4b shows the energy dispersion of edge states in the absence of spin degeneracy in 2D TI, forming a 1D Dirac cone

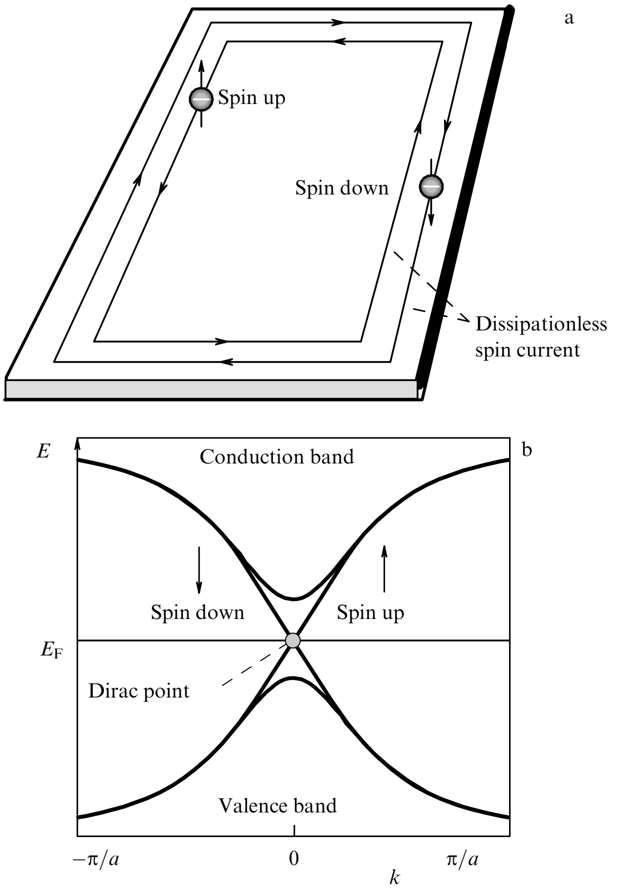

Figure 4. System with the quantum spin Hall effect. (a) Schematic of a pair of spin-selective 1D helical states in a 2D TI in real space. Dissipationless spin current flows along the edges in the presence of the electric field. The directions of electron flows are opposite and are defined by the up or down spin orientation [9]. (b) Dispersion of the edge state energy in the absence of spin degeneracy for a 2D TI, forming a 'one-dimensional' Dirac cone [8].

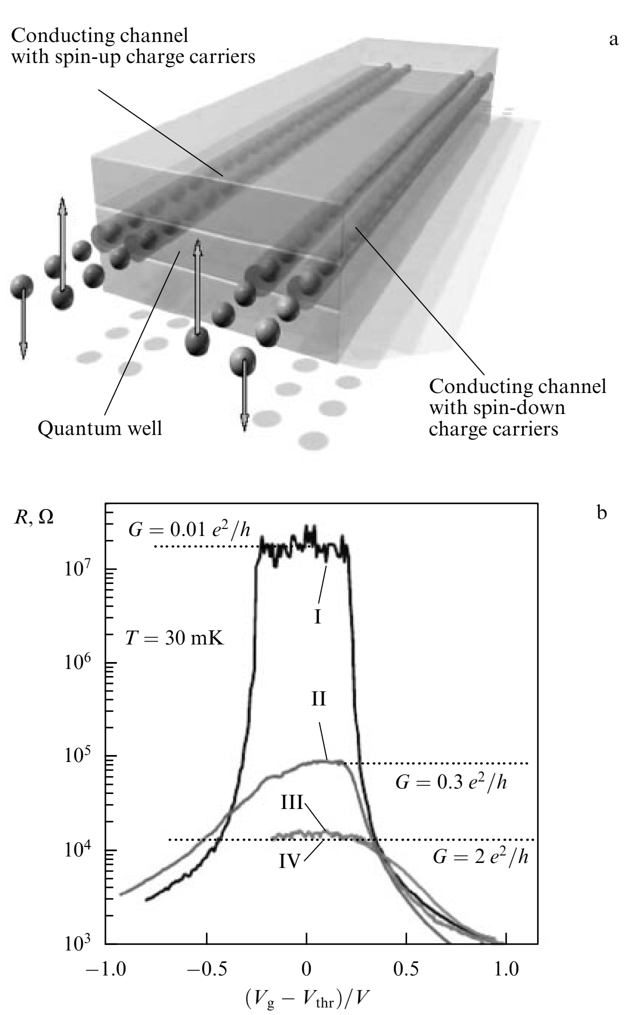

Figure 5. Quantum spin Hall insulator. (a) Schematic of edge channels with polarized spins in a quantum well. (b) Resistances of quantum wells with various HgTe layer thicknesses versus the gate voltage V_g. I — structure with a normal electron state ($d = 5.5$ nm); II, III, and IV — structures with an inverted electron state ($d = 7.3$ nm); G — conductance. The threshold voltage V_{thr} was defined such that the quantum spin Hall effect would be observed in the vicinity of $V_g = V_{thr}$ [10].

[8]. Such edge states were named helical states in [26], similarly to the 'helicity' quantum number that defines the correlation between spin and momentum of a particle. Usually, systems with such a spin state are said to have the helical polarization of the spin or spin–momentum synchronization, such that the spins align according to the momentum direction. In a gapless edge state, just as in the case of graphene, such electrons act as 1D massless Dirac fermions inside the gap. Kane and Mele discovered a very important fact that the electron states in their quantum spin Hall insulator model are characterized by a new topology associated with a Z_2 index [25], which determines whether there is an even or odd number of crossings between the 1D edge state and the Fermi level in the range from 0 to π/a, where a is the lattice constant. In other words, this index allows performing a topological classification based on parity, which we describe in Section 1.3. Unfortunately, due to the weakness of spin–orbit coupling and scattering on impurities, which should lead to dissipation, it is difficult to observe the quantum spin Hall effect experimentally based on the Kane–Mele model.

Soon after the appearance of papers [24, 25], Bernevig, Hughes, and Zhang [27] suggested another way to realize the quantum spin Hall effect with topological properties and showed that with a change in the width of a semiconductor quantum well in HgTe/CdTe, its usual electron state transforms into the 'inverted' state at some critical width. Such a transformation is a topological quantum phase transition from a normal insulator phase to the phase with the quantum spin Hall effect and with one pair of helical edge states.

Following these theoretical predictions, König and colleagues [10, 28] measured the electrical conductivity caused by edge states in CdTe/HgTe/CdTe quantum wells and observed a decrease in the band gap as the width d of the HgTe layer in the quantum well was increased. At a critical thickness $d_c = 6.3$ nm, the gap closed, which corresponded to the phase transition between the state with a normal insulator phase for $d < d_c$ and the state with the quantum spin hall effect for $d > d_c$. Structures with narrow quantum wells and a normal electron state with the Fermi level inside the gap demonstrated zero conductivity. Quantum wells with the inverted electron state demonstrated conductivity that was close to the expected value for the transport through edge channels of a quantum spin Hall insulator (Fig. 5). These results prove that transport in the quantum spin Hall regime is indeed caused by the gapless edge state. We note that the structures under investigation had dimensions less than the mean free path for inelastic collisions (~ 1 μm) in order to minimize the scattering on impurities and decrease the spin current dissipation. In the quantum spin Hall regime, structures with a two-fold thickness difference had the same resistance. This clearly indicated that in cases III and IV shown in Fig. 5, where $G = 2e^2/h$, the conductivity is defined by the edge state that is independent of the sample width [1].

We note that the band inversion mechanism in HgTe/CdTe quantum wells was studied in [29], although it was not related to TIs and appeared long before the publication of papers [10, 28].

1.3 Three-dimensional topological insulators

In 2006, three theoretical groups simultaneously showed that although the quantum Hall effect cannot be observed in a 3D state, the topological characteristics of states in a quantum spin Hall insulator or a 2D TI can be naturally generalized to a 3D TI [13, 30, 31]. The authors demonstrated a connection between the bulk state with an insulator band gap and a gapless conducting surface state protected by T symmetry.

The possibility of creating 'weak' and 'strong' 3D TIs was discussed in [30, 32]. Simple 3D TIs can be created as a structure composed of 2D quantum spin Hall insulator layers in analogy with the suggested 3D quantum Hall state [33]. The helical edge state in this case becomes an anisotropic surface state. However, in such a structure, due to the weak coupling between the layers and a weak spin–orbit coupling, the band gap induced by these couplings must be small and the resulting state turns out to be unstable with respect to disorder. Such a structure is attributed to weak 3D TIs.

A strong 3D TI has many similarities with a 2D TI in the sense that the strong 3D TI is a combination of a conventional insulator with a topological one under continuous interpolation. To create such a TI, strong spin–orbit coupling is needed. The surface state in a strong 3D TI forms a unique two-dimensional 'topological metal'. Unlike the sate of a conventional metal, which has both up and down spins at every point of the Fermi surface, the surface state in a strong 3D TI is not spin-degenerate. This nontrivial topological state of a 3D TI has an insulator band gap in the bulk and a gapless surface state formed by an odd number of Dirac states. Such a state is protected by time-reversal symmetry from back-scattering on defects. This means that, due to the helical spin polarization, the back scattering from the momentum **k**-space to the momentum −**k**-space is forbidden. A surface state in which the electron spin is perpendicular to the momentum lies mainly in the plane of the sample surface [1, 2]. Electrons in this state, as on the 2D TI edges, can move in directions along the surface of the bulk material almost without energy dissipation, as shown in Fig. 6a. If the time reversal symmetry is not broken in the bulk but is violated on the surface, the material completely becomes an insulator, both in the bulk and on the surface. An unusual metal that forms on the TI surface inherits the topological properties of the bulk insulator.

The existence of disorder or impurities on the surface should lead to back-scattering, but the topological properties of a bulk insulator prevent the destruction of the metallic surface state; band gap formation or localization is impossible [3]. In other words, the metallic surface state formed due to nontrivial topology cannot be changed as long as the material in the bulk remains an insulator with a band gap. Dirac fermions in a 3D TI, just as in a 2D TI, are characterized by a linear dependence of energy on momentum, which now has the form of Dirac cones with vertices at the Dirac point (Fig. 6b). Combined data of angle-resolved photoemission spectroscopy (ARPES) [34] and scanning tunneling spectroscopy [35] for Bi_2Se_3 and Bi_2Te_3 have shown a linear density of states, as expected for the linear Dirac dispersion, but only in a small region near the Fermi level. The rest of the density of states was curved.

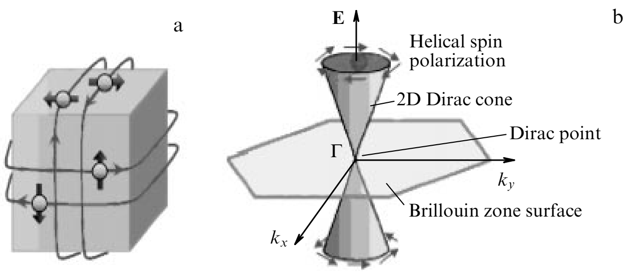

Figure 6. Surface state of a 3D TI with the Dirac dispersion. (a) Schematic illustration of 2D helical surface state in real space. (b) Energy dispersion of a nondegenerate spin surface state of a 3D TI, forming 2D Dirac cones. Due to the helical spin polarization, back-scattering from **k**-space to −**k**-space is impossible [2].

Electrons in a gapless surface state act as massless fermions inside the insulator band gap. Their properties, just as the properties of 2D TIs, are described by the Dirac equation, in which the energy eigenvalue for a free particle with mass m has the form

$$E = \pm c\sqrt{p^2 + m^2c^2}\,. \tag{1}$$

It can be seen that the Dirac equation corresponds to positive- and negative-energy states and the energy eigenvalue has a band gap for a finite mass but becomes gapless when $m = 0$. Therefore, gapless systems that satisfy the Dirac equation are called massless. If the effective mass were defined as the second energy derivative $\mathrm{d}^2E/\mathrm{d}k^2$ with respect to the wave vector, the expression for the effective mass

$$m^* = \hbar^2\left(\frac{\mathrm{d}^2E}{\mathrm{d}k^2}\right)^{-1} \tag{2}$$

would be divergent [2]. (It may be helpful to recall that $p = \hbar k$.)

The theory in [36] predicts that because the T symmetry in a TI requires that states with momenta **k** and −**k** have oppositely directed spins, the electron spin must rotate through 2π as the electron circulates around the Dirac point in the momentum space, and the electron wave function must acquire a nonzero geometrical quantum Berry phase (Fig. 6b). For linear dispersion in a 3D TI near the Dirac point, the Berry phase is $\gamma = \pi$ [37], while metals with conventional spin–orbit coupling, such as gold, have a zero Berry phase.

The most important property of a topological surface state in a 3D TI is that it is topologically protected. There are three aspects to the term 'topological protection' [2]. The first is a consequence of the new topology defined by the fundamental topological index Z_2 mentioned above. In a 3D TI, Z_2-topology guaranties the existence of a gapless surface state as long as the time-reversal symmetry is preserved. (In order to fully characterize a 3D system, four Z_2-invariants are needed.) The second aspect is related to the helical spin polarization, which forces electrons with momenta **k** and −**k** to have oppositely directed spins. The third aspect is defined by the Berry phase π, which corresponds to Dirac massless fermions and prevents their weak localization via destructive interference of paths reversed in time.

We note that a combination of a 3D TI and a conventional superconductor can transform the spin state considered here into a correlated state at the interface between them and can lead to the formation of predicted Majorana fermion excitations and a topological superconductor [38].

A list of more than 30 TIs (binary and ternary compounds based on Bi, Sb, Se, Te, Tl, Sn, and Pb) studied experimentally is given in [2], although a much larger number of compounds were predicted to be TIs, but have not been studied experimentally. In Section 2, we discuss the results of experimental investigations of TIs mostly based on Bi, Te, and Tl, because the characteristic TI properties are more clearly pronounced in these materials.

2. Results of experimental investigations of topological insulators

Before we start analyzing experimental TI investigations, we briefly discuss verification methods that can show whether the material under study is indeed a TI.

In the case of 2D TIs, it must be verified that a 1D helical edge state exists, which can be done only in quantum transport experiments with nanostructures. In papers [10, 28] discussed in Section 1, the existence of edge states was verified by measuring the quantized conductivity of quantum wells. Later, the quantum spin Hall effect was directly observed in [39], where spin transport was studied in HgTe quantum wells by using them as a spin current injector and as a spin Hall effect detector, which allowed observing the helical spin polarization.

Surface states in 3D TIs were successfully studied using ARPES, spin-resolved photoemission spectroscopy (SRPES) [40, 41], and scanning tunneling spectroscopy [35, 42]. In some works, the existence of metallic surface and coherent surface states was confirmed experimentally by using optical spectroscopy and measuring optical conductance [43–47].

Results of topological transport investigations in 3D TIs, which are discussed in what follows, are still ambiguous. ARPES is one of the main methods for measuring the parameters of the Fermi surface and investigating the electron properties of a solid (band structure, electron interaction, and so on). In ARPES experiments, the sample is illuminated by high-energy photons, which cause the emission of photoelectrons from the occupied states. By measuring the angle and energy distributions of emitted photoelectrons, information on the initial electron distribution over energy and momentum can be obtained if the energy of incident photons is known. In the case of SRPES experiments, the energy analyzer is replaced by a Mott spin detector, which allows measuring the distribution of the electron spin orientation over the Fermi surface. This distribution can be used to estimate the Berry phase on the surface [1] and, in particular, to separate spin-polarized electron beams into two channels: with spin-up and spin-down electrons. For 3D TIs, the ARPES and SRPES experiments were the most convincing; the authors not only observed the Dirac cone but also showed that this cone is nondegenerate and has a helical spin polarization. The theoretical prediction in [32] that the $Bi_{1-x}Sb_x$ compound is a 3D TI in the insulator state was soon confirmed experimentally using ARPES [48]. This compound was the first experimentally identified 3D TI. Direct observation of helical spin polarization of the $Bi_{1-x}Sb_x$ surface state was performed in SRPES experiments [49, 50].

However, the $Bi_{1-x}Sb_x$ compound was not very suitable for use as a TI in real spintronic devices because this compound had a small band gap in the bulk and its samples contained many defects caused by disorder [51]. Therefore, the search for disorder-free topological phases was continued in stoichiometric compounds with a large band gap, with the aim to use them as a matrix material for the study of various topological phenomena. It was soon predicted in [52] that long-known thermoelectric compounds Bi_2X_3 (where $X = $ Se, Te) should be 3D TIs. These compounds, being the simplest 3D TIs, have been thoroughly studied using ARPES and SRPES experiments over recent years. The results of the investigations most likely confirm the existence of a 2D surface state in Bi_2X_3 (see, e.g., [1]).

We first consider Bi_2Se_3 because it has a simple band structure and a relatively large band gap (~ 0.3 eV). High-purity Bi_2Se_3 samples show stable behavior inherent to TIs at temperatures up to room temperature [53], which indicates good prospects for future applications. This layered compound with a rhombohedral lattice is a package of weakly bound Se–Bi–Se–Bi–Se quintuples, each 1 nm thick. The elementary cell consists of three quintets [54], and the Fermi surface of a Bi_2Se_3 sample is an ellipsoid. Due to the layered structure, the resistance of Bi_2Se_3 samples is anisotropic, with the ratio $\rho_{zz}/\rho_{xx} \approx 10$ [55]. Large crystals can easily crack along the quintet edges, and hence it is not hard to obtain single crystals with a mirror surface and an area of 10×5 mm^2. As an example, Fig. 7 shows Bi_2Se_3 and Bi_2Te_3 single crystals respectively doped by Cu and Sn before exfoliation [56]. Figure 8 shows a schematic diagram of the Bi_2Se_3 3D Brillouin zone, its 2D surface projection (111), and a topological surface state in Bi_2Se_3 measured in ARPES experiments [51]. Quite similar results are obtained in ARPES experiments with 3D TIs such as Bi_2Te_3, Sb_2Se_3, and Sb_2Te_3 [1].

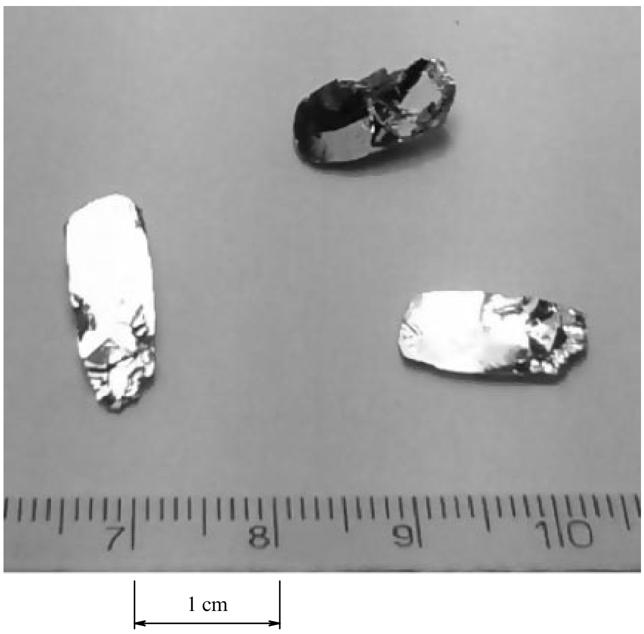

Figurre 7. $Bi_{2-x}Cu_xSe_3$ and $Bi_{2-x}Sn_xTe_3$ single crystals cut from ingots before exfoliation [56].

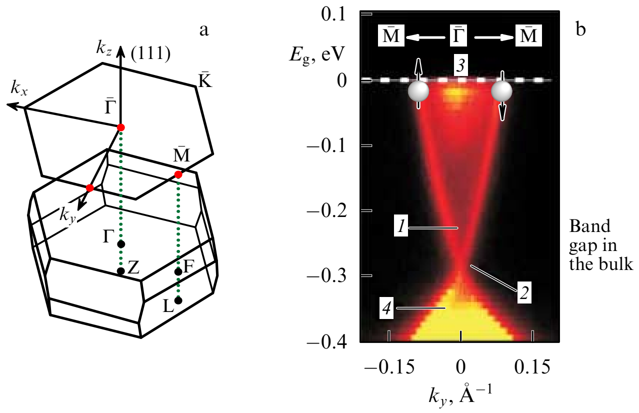

Figure 8. (Color online.) Characteristic evidence of a metallic surface state in a Bi_2Se_3 3D TI. (a) Schematic diagram of the 3D hexagonal Brillouin zone of Bi_2Se_3 and its 2D surface projection (111), where $\bar{\Gamma}$ is the Brillouin zone center and $\bar{M}$ is the middle of the Brillouin zone edge. (b) Electron structure of Bi_2Se_3 measured by high-resolution ARPES. The image shows the dependence of the electron energy E_g on the momentum k_y along the $\bar{M}-\bar{\Gamma}-\bar{M}$ direction (white arrows). The V shape of a linear dispersion law is due to the existence of surface state band *1* inside the bulk gap. The top of the V-shaped linear dispersion is the Dirac point *2*, *3* is the bulk conduction band, and *4* is the bulk valence band. The dark part in the surface state band and the upper part of the valence bad (in [51], the original image in Fig. 1a is bright yellow) indicate a high density of states. Electron spin directions are shown by vertical arrows [51].

It was later shown in [57] that the topological surface state in Bi_2Se_3 has a much larger degree of spin polarization (around 0.75) than was found in previous experiments with the same compound, and the polarization limits are mostly due to external factors.

However, not all materials can be studied in ARPES experiments because the samples must have a very clean flat surface. If ARPES is not possible, charge transfer experiments can be convenient. Furthermore, the lack of information about transport and, especially, mobility in 3D TIs was a serious problem during their study. The measurement of surface currents is the first key step in the study of Majorana fermions [58] or the peculiar electrodynamics of TIs [59].

Measurements of quantum oscillations of resistance — the Shubnikov–de Haas (SdH) effect — and of magnetization — the de Haas–van Alphen (dHvA) effect — could confirm the existence of conducting surface states in 3D TIs.

It is known that the SdH effect is widely used in studying the Fermi surface structure in metals and semiconductors. Landau quantization associated with the semiclassical cyclotron motion of electrons in a magnetic field can reveal the difference between conventional and Dirac electrons. In both cases, the density of states becomes a periodic function inversely proportional to the magnetic field, which leads to SdH oscillations [60]. But because the oscillations associated with the Landau levels of a 2D Fermi surface must depend only on the perpendicular component of the magnetic field $B_\perp = B\cos\theta$, by rotating the sample in the magnetic field we can distinguish those oscillations from 3D oscillations related to bulk carriers. Here, θ is the angle between the magnetic field direction **B** and the crystallographic c axis perpendicular to the sample surface, which is schematically shown below on the inset in Fig. 11b. Moreover, the phase term in 2D oscillations directly represents the Berry phase of the system and therefore allows confirming the connection of observed oscillations with Dirac fermions. In TIs, the conductance σ_{xx} for oscillations in the magnetic field can be written as

$$\Delta\sigma_{xx}^{(N)} \propto \cos\left[2\pi\left(\frac{F}{B_N} - \frac{1}{2} + \beta\right)\right], \tag{3}$$

where F is the oscillation frequency, B_N is the magnetic field at the Nth extremum of $\Delta\sigma_{xx}$, and $\beta = \gamma/2\pi$. For Dirac fermions, according to the theory, $\beta = 1/2$, whence the Berry phase is $\gamma = \pi$ (see, e.g., [61]).

Due to these reasons, after the ARPES experiments with $Bi_{1-x}Sb_x$ [48, 49], studies of this compound in SdH and dHvA experiments began [62]. Unfortunately, the charge transfer experiments, which were successful in the case of 2D TIs, turned out to be complicated in 3D materials, because if the Fermi level in the insulator was located inside the bulk band gap near the conduction band, then the contribution to the conductivity associated with bulk carriers would always dominate the contribution from the surface conductivity [63–66].

The problem is that bismuth chalcogenides Bi_2Se_3 and Bi_2Te_3 are actually not insulators: they are in fact relatively good metals. Usually, it turns out that after growing, the Bi_2Se_3 and Bi_2Te_3 single crystals have n-type conductivity with the concentration of carriers in the bulk $n \sim 10^{19}$ cm^{-3} [51, 63–65, 67]. Their Fermi level is located at the edge of the conducting band and they have high conductivity with a 'metallic' dependence of resistance on temperature. It followed from the ARPES experiments and first transport experiments (see, e.g., [1, 2, 64]) that in order to observe 2D surface states in 3D TIs, samples with n not greater than 10^{17} cm^{-3} were needed, and hence a series of attempts were made to control the location of the Fermi level inside the bulk band gap and move it closer to the Dirac point of the surface state. This helped to decrease the charge concentration and conductivity of the samples, transforming them into insulators.

In [68, 69], Bi_2Se_3 was doped by Cd or Ca, and the variation of x in $Bi_{2-x}Cd_xSe_3$ or $Ca_xBi_2Se_3$ led to a Fermi level shift from the conduction band inside the bulk band gap and then into the valence band. It was shown in [70] that changing the Sn concentration in $(Bi_{1-\delta}Sn_\delta)Te_3$ allows shifting the Fermi level such that it intersects only surface states in the bulk band gap. Some authors replaced binary bismuth chalcogenides in their studies with ternary compounds like Bi_2Te_2Se [71–73]. Quite recently, it was shown that charge concentration in Bi_2Se_3 can be increased by copper intercalation [74].

In [63], among many Bi_2Te_3 crystals obtained from a grown ingot, there were both 'metallic' and 'nonmetallic' samples with different charge concentrations. Figure 9, taken from [63], shows temperature dependences of the longitudinal resistivity ρ_{xx} for four Bi_2Te_3 samples with different charge concentrations. In nonmetallic samples Q1, Q2, and Q3, the resistance increased as the temperature decreased, reaching saturation at low temperatures with a resistance ~ 50 times higher than in the metallic sample N1. Hall measurements have shown that the bulk carrier concentration in nonmetallic samples did not exceed $\sim 7\times10^{15}$ cm^{-3}, while for the sample N1 it was much higher.

The authors of [63], when investigating the SdH oscillations in nonmetallic samples, confirmed the existence of a 2D surface state in them. Figure 9b shows the derivatives $d\rho_{xx}/dB$ versus the inverse magnetic field perpendicular component $1/B_\perp = 1/B\cos\theta$, measured in sample Q1. Dashed lines indicate the positions of maxima on the curves. The lower part of Fig. 9b shows the θ dependence of the third

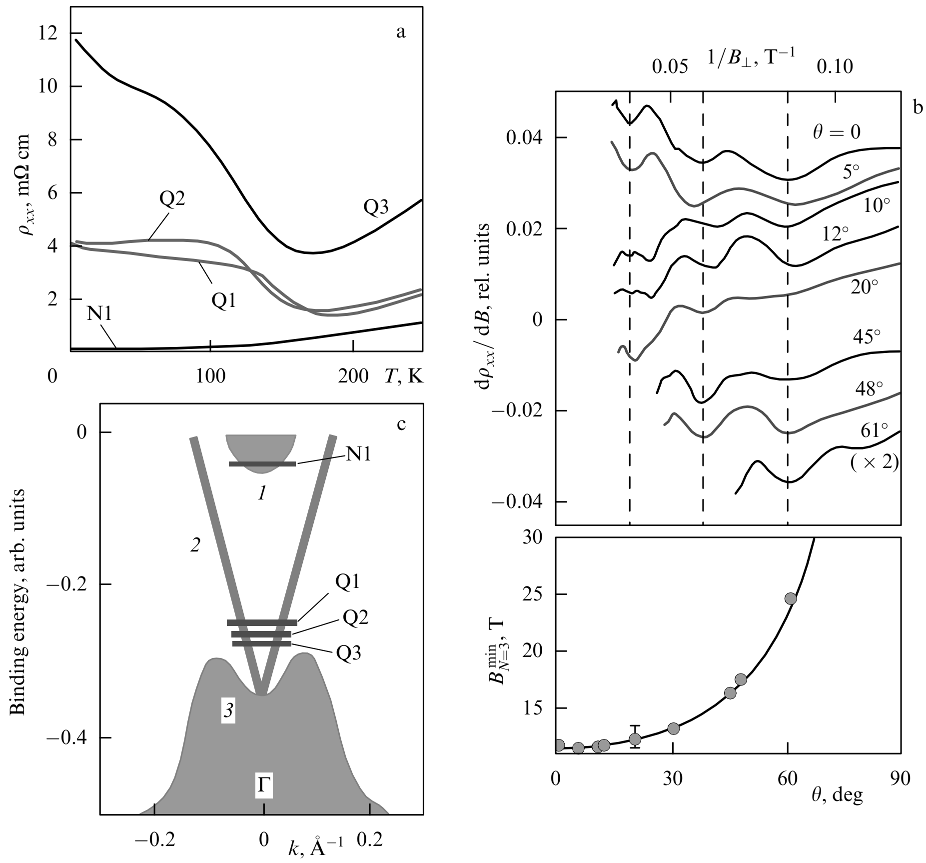

Figure 9. (a) Temperature dependences of longitudinal resistivities ρ_{xx} for four Bi_2Te_3 samples with different carrier concentrations. In nonmetallic samples Q1, Q2, and Q3, the resistance increased as the temperature decreased, reaching saturation at low temperatures with the resistance 50 times higher than in the metallic sample N1. (b) Derivatives $d\rho_{xx}/dB$ versus the inverse value of the magnetic field perpendicular component $1/B_\perp = 1/B\cos\theta$, measured in the sample Q1 (θ is the angle between the magnetic field direction **H** and the c axis, which is perpendicular to the sample surface). Dashed lines indicate the positions of minima on the curves. The lower part shows the third oscillation minimum position ($B_{N=3}^{min}$) on the B axis (dots) and the value of θ (solid curve) versus the angle $1/\cos\theta$. It is clear that the oscillations depend only on $B_\perp$, as it should be in the case of a 2D Fermi surface. (c) Schematic illustration of surface state dispersion near the Γ point based on the data in [70]: *1* — bulk conduction band, *2* — surface state band, *3* — bulk valence band. Positions of the Fermi levels in the samples from [63] are indicated by horizontal segments.

oscillation minimum position on the B axis (dots) and the value of $1/\cos\theta$ (solid curve). It is clear that the oscillations depend only on $B_\perp$, as it should be in the case of a 2D Fermi surface. At angles $\theta > 65°$, oscillations were not observed. SdH oscillations were observed in the metallic sample N1 at angles up to $\theta = 90°$ and the positions of the oscillation amplitude minima strongly deviated from the $1/\cos\theta$ dependence, which, as the authors of [63] believed, indicated a connection between these oscillations and the 3D Fermi surface. It was also obtained in [65] that only 3D SdH oscillations can be observed in Bi_2Se_3 with $n = 5 \times 10^{18}$ cm^{-3}. Figure 9c shows the dispersion layout of surface states near the Γ point, built based on the data in [70]. The Fermi energy positions in the studied samples [63] are indicated with horizontal segments. As we can see from the results presented in Fig. 9, the transport experiments can seriously complement the ARPES experiments.

In studying SdH oscillations in conventional metals, the connection between the Landau level index N and the area of the extremal cross section of the Fermi surface in **k**-space is expressed as

$$2\pi(N + \delta) = S_F \frac{\hbar}{eB}, \quad (4)$$

where the Onsager phase correction is $\delta = 1/2$ [58, 75]. The dependence of the positions of ρ_{xx} minima and maxima in the inverse magnetic field $1/B$ on the corresponding Landau level indices N for $\theta = 0$ was extrapolated in [63] to higher fields. The result shows that for nonmetallic crystals, the Berry phase is in the range $0 < \gamma < 1/2$.

The findings in [76] were not suggested by the preceding results: the authors studied magnetotransport in Bi_2Se_3 samples with a high bulk carrier concentration $n = 4.7 \times 10^{19}$ cm^{-3} and expected 3D transport domination. As it should be for such a concentration n, the temperature dependence of the resistance had a metallic character. But instead of bulk SdH oscillations, only 2D oscillations were observed, being periodic in the inverse magnetic field. A Fourier analysis of the oscillations indicated only one frequency.

Figure 10 shows the dependence of the longitudinal resistance R_{xx} on the magnetic field, measured for different tilt angles θ of a sample with respect to the magnetic field. It is clear that in the case of Bi_2Se_3 with a high bulk concentration n, the oscillation amplitude is much higher than in [63], and these oscillations can be studied without using the derivatives dR_{xx}/dB. As can be seen from Fig. 10, the oscillations were not observed at angles $\theta > 60°$. The inset shows that as θ varies (dots), the position of the 13th R_{xx} minimum (marked with arrows) follows the $B_{13}(\theta = 0)/\cos\theta$ dependence (solid curve), and therefore depends only on the perpendicular component of the magnetic field. As the temperature

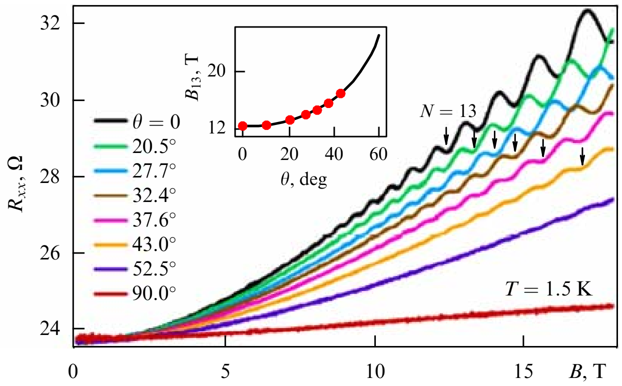

Figure 10. (Color online.) Longitudinal resistance R_{xx} of a Bi_2Se_3 single crystal versus the magnetic field measured for various sample tilt angles θ with respect to the magnetic field direction. The inset shows that the position of the 13th R_{xx} minimum (marked in the figure with arrows) with θ variation (dots) follows the $B_{13}(\theta = 0)/\cos\theta$ dependence (solid curve), which means that it depends only on the perpendicular component of the magnetic field [76].

increased, the oscillation amplitude decreased and the oscillation disappeared at $T > 50$ K. As was noted above, such dependences are characteristic of SdH 2D oscillations, which occur in surface layers of 3D TIs with $n \sim 10^{16}-10^{17}$ cm^{-3}.

It is known that by measuring the temperature dependence of SdH oscillations, the main kinetic parameters associated with the system conductivity can be found using the Lifshitz–Kosevich relation [60]

$$\Delta R_{xx}(T, B) \propto \frac{\alpha T/\Delta E_N(B)}{\sinh(\alpha T/\Delta E_N(B))} \exp\left(-\frac{\alpha T_{\rm D}}{\Delta E_N(B)}\right), \quad (5)$$

where $\Delta E(B) = heB/(2\pi m_{\rm eff}^{\rm 2D})$ is the difference between adjacent Landau level energies, $m_{\rm eff}^{\rm 2D}$ is the carrier effective mass, $\alpha = 2\pi^2 k_{\rm B}$, $k_{\rm B}$ is the Boltzmann constant, and e is the free electron charge. In this case, we obtain the relative oscillation amplitude

$$\frac{\Delta R}{\Delta R_0} = \frac{T \sinh\left(\alpha T/\Delta E_N(B_{\rm min})\right)}{T_0 \sinh\left(\alpha T_0/\Delta E_N(B_{\rm min})\right)} \,. \quad (6)$$

From the $\Delta R/\Delta R_0$ temperature dependences, for every $B_{\rm min}$, we can find the energy difference, and from the tangent to the semilogarithmic dependence of $D = \Delta RB \sinh(\alpha T/\Delta E)$ on $1/B$, we can determine the Dingle temperature $T_{\rm D} = h/(4\pi^2 \tau_{\rm D} k_{\rm B})$ [K]. The value of $T_{\rm D}$ can be used to find $m_{\rm eff}^{\rm 2D}$ and the relaxation time $\tau_{\rm D} = h/(4\pi^2 T_{\rm D} k_{\rm B})$, which turns out to be two to three times shorter than that measured previously in samples with $n \sim 5 \times 10^{18}$ cm^{-3} [65]. Such a decrease in the time $\tau_{\rm D}$ is connected, as the authors of [76] believe, with a large number of impurities (Se vacancies). Using the SdH oscillation period $F = (\hbar/2\pi e)\, S_{\rm F}$ [60], where $S_{\rm F} = \pi k_{\rm F}^2$ is the Fermi-surface extremal cross section (under the assumption that the Dirac cone is isotropic), we can find the Fermi wave vector $k_{\rm F}$, the Fermi velocity $v_{\rm F} = \hbar k_{\rm F}/m_{\rm eff}^{\rm 2D}$, and the electron mean free path $l_{\rm F} = v_{\rm F}\tau$. The values of these parameters are shown in Table 1. The results in [76] were explained by the existence in a highly doped n-type 3D sample with parallel transport through many channels, each acting as a 2D electron system. To substantiate this explanation, the authors of [76] employed the 'bulk quantum Hall effect' observed by them. Regarding the data from previous studies of Bi_2Se_3 TIs with lower bulk carrier concentrations [64, 65, 67, 77–79], the authors of [76] assumed that Bi_2Se_3 has rich electron properties with a 'dimensional crossover' in the magnetotransport behavior (from 2D to 3D and then back to 2D) depending on n. For very low n ($\sim 10^{17}$ cm^{-3}), the bulk conductivity vanishes and 2D surface transport is observed in the TI [64]. For intermediate values of n ($\sim 10^{17}-10^{19}$ cm^{-3}), the bulk transport with 3D SdH oscillations prevails [65, 67, 77–79]. For very high n ($\gtrsim 3 \times 10^{19}$ cm^{-3}), as in the discussed paper [76], the dominating bulk transport exhibits 2D SdH oscillations because the sample contains many 2D conductive channels.

However, the assumption made by the authors of [76] about the bulk transport domination with 3D SdH oscillations for the intermediate values $n \sim 10^{17}-10^{19}$ cm^{-3} turned out to be ambiguous. Soon after the publication of [76], quantum oscillations were studied in $Bi_{2-x}Sn_xTe_3$ and $Bi_{2-x}Cu_xSe_3$ single crystals with $n \approx (3-5) \times 10^{18}$ cm^{-3}, demonstrating a metallic dependence of resistance on temperature [56]. (The study of $Bi_{2-x}Cu_xSe_3$ single crystals was of special interest, because the Bi_2Se_3 3D TI doped with

Table 1. Parameters of 2D systems* for samples from [76, 82, 86, 87].

Parameter \ Sample	$Bi_{2-x}Cu_xSe_3$ [86] 1	$Bi_{2-x}Cu_xSe_3$ [86] 2	$Bi_{2-x}Cu_xSe_3$ [86] 3	$Cu_{0.25}Bi_2Se_3$ [82]	Bi_2Se_3 [76]	Bi_2Se_3, film [87]
$n \times 10^{19}$, cm^{-3}	−2.8	−11	−12	−4.3	−4.7	—
$F_{\rm s}$, T	287	330	300	325	162	106.8
$n_{\rm 2D} \times 10^{13}$, cm^{-2}	1.4	1.6	1.5	—	0.78	0.26
$k_{\rm F}$, nm^{-1}	0.94	1.01	0.97	0.97; 1.3	—	0.57
$m_{\rm eff}^{\rm 2D}/m_{\rm e}$	0.16	0.18	—	0.194	0.14	0.2
$T_{\rm D}$, K	21.8	23.6	—	23.5	25	—
$\tau_{\rm D} \times 10^{-14}$, s	5.6	5.2	—	5.2	5	—
$\mu_{\rm eff}^{\rm 2D}$, cm^2 V^{-1} s^{-1}	614	513	—	—	620	1330
$v_{\rm F} \times 10^5$, m s^{-1}	6.8	6.4	—	5.8	5.7**	3.3
$\ell_{\rm F}$, nm	38	34	—	30	29**	—
γ	π	0.9π	1.4π	—	~ 0	0.8π

* $F_{\rm s}$ — 2D oscillation frequency, $n_{\rm 2D}$ — carrier concentration, $k_{\rm F}$ — Fermi wave vector, $m_{\rm eff}^{\rm 2D}$ — carrier effective mass, $m_{\rm e}$ — free electron mass, $T_{\rm D}$ — Dingle temperature, $\tau_{\rm D}$ — relaxation time, $\mu_{\rm eff}^{\rm 2D}$ — effective mobility, $v_{\rm F}$ — Fermi velocity, $\ell_{\rm F}$ — mean free path, γ — Berry phase, n — bulk carrier concentration.

** Data from [81].

copper exhibited superconductivity at a temperature of 3.6–3.8 K [80, 81], which gave reason to believe that this TI can become the first topological superconductor [74]). Indeed, $Bi_{2-x}Sn_xTe_3$ samples demonstrated oscillations caused only by bulk 3D carriers from the conduction band. Although these oscillations depended on the sample tilt angle with respect to the magnetic field θ, their amplitude decreased insignificantly with increasing θ. Positions of the oscillation amplitude extrema on the B axis strongly deviated from the 2D dependence on the angle θ, which was expected for the 2D surface conductivity, while the $Bi_{2-x}Cu_xSe_3$ samples demonstrated only 2D SdH oscillations. Most likely, the introduction of copper into Bi_2Se_3 not only increases the carrier concentration, as was noted in [74], but also leads to the formation of multiple 2D channels [76] and changes some kinetic parameters.

Here, we first discuss magnetotransport studies of Bi_2Se_3 doped with copper [82]. This layered compound allows both copper intercalation between Se layers and random substitution of Bi with copper, respectively resulting in $Cu_xBi_2Se_3$ or $Bi_{2-x}Cu_xSe_3$. The result greatly depends on the single crystal growing conditions (see [81] and the references therein). The authors of [82] studied dHvA quantum oscillations in $Cu_{0.25}Bi_2Se_3$ and Bi_2Se_3 samples using torque magnetometry in magnetic fields up to 8 T. It was discovered that doping the samples with copper not only increases the carrier concentration but also affects the Fermi surface shape. At the same time, v_F, τ_D, and l_F remain almost unchanged. When studying the oscillation dependence on the angle between the magnetic field and the sample surface in $Cu_{0.25}Bi_2Se_3$ and Bi_2Se_3 crystals, the oscillations were observed only at angles less than 35°, just as in previous studies of Bi_2Se_3 performed by other authors. However, the authors of [82] made an assumption that these oscillations are bulk ones, because the angular dependence of their frequency can be connected with the area variation of the 3D ellipsoidal Fermi surface cross section during a change in the carrier concentration. Based on this assumption, the authors deduced the Fermi wave vectors $k_F^x = k_F^y = 0.97$ nm^{-1} for the minor ellipsoid axes and $k_F^z = 1.3$ nm^{-1} for the major ellipsoid axis in $Cu_{0.25}Bi_2Se_3$. The angular dependence of the oscillation frequency in the Bi_2Se_3 sample was used to find $k_F^x = k_F^y = 0.69$ and $k_F^z = 1.2$ nm^{-1}. Based on the cross-sectional area, these values were used to obtain the respective bulk carrier concentrations $n = (1/3\pi^2)\, k_F^x k_F^y k_F^z = 4.3 \times 10^{19}$ cm^{-3} and 1.8×10^{19} cm^{-3} in $Cu_{0.25}Bi_2Se_3$ and Bi_2Se_3. The main kinetic parameters of these systems shown in Table 1 were obtained from the periods and temperature dependences of SdH oscillations.

Immediately after the appearance of [82], Lahoud and coauthors [83] used ARPES and the SdH effect and also investigated the evolution of the Fermi surface shape in Bi_2Se_3 with the variation of the bulk carrier concentration. Experiments were performed with nonstoichiometric samples of $Bi_{2-x}Se_{3+y}$ with $n \approx 10^{17} - 10^{19}$ cm^{-3} and a Bi_2Se_3 copper-doped sample with $n \approx 10^{20}$ cm^{-3}. ARPES experiments have shown that the Dirac surface state exists in the entire range of concentration variation. As n was increased, the Dirac dispersion was preserved, but the Dirac point shifted toward lower energies, leaving the Fermi velocity unchanged. Figure 11a shows the ARPES data obtained with a copper-doped Bi_2Se_3 sample with $n \approx 4 \times 10^{20}$ cm^{-3}. We can clearly see the surface state with the Dirac point at an energy approximately 0.5 eV lower than the Fermi level. Two branches of the surface state linear dispersion 'enclose' the bulk parabolic band.

Figure 11b shows the longitudinal resistance of a copper-doped Bi_2Se_3 sample with $n \approx 10^{20}$ cm^{-3} as a function of the magnetic field, measured at different angles θ between the magnetic field and the sample axis c (see the inset in Fig. 11b). Oscillations were visible at temperatures up to 49 K and the temperature dependence of their amplitude was used to calculate the value $m_{\mathrm{eff}}^{2D} \approx 0.24 m_e$, where m_e is the free electron mass. Based on the measurement data of SdH oscillations, the authors of [83] reconstructed the Fermi surface and showed that with an increase in n the Fermi surface transforms from a closed ellipsoid in samples with $n \approx 10^{18}$ and 10^{19} cm^{-3} to an open cylinder in a sample with $n \approx 10^{20}$ cm^{-3}.

SdH oscillations measured in a Bi_2Se_3 sample with $n \approx 10^{17}$ cm^{-3} for different tilt angles θ are shown in Fig. 12a. It is interesting that the oscillation amplitude is very small

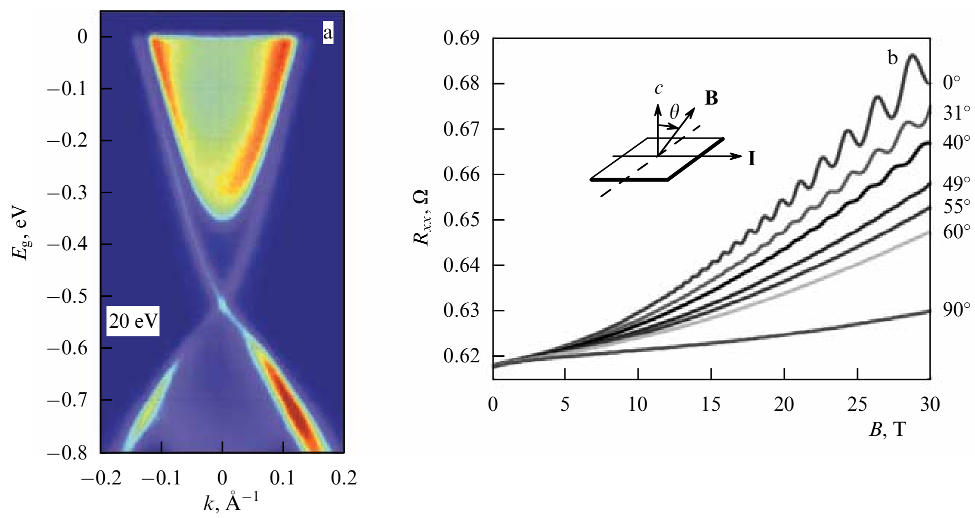

Figure 11. (a) ARPES data obtained for a copper-doped Bi_2Se_3 sample with $n \approx 4 \times 10^{20}$ cm^{-3}. (b) Longitudinal resistance as a function of the magnetic field measured for different tilt angles θ between the magnetic field and the sample with $n \approx 10^{20}$ cm^{-3} at a temperature of 4.2 K (schematically shown in the inset) [83].

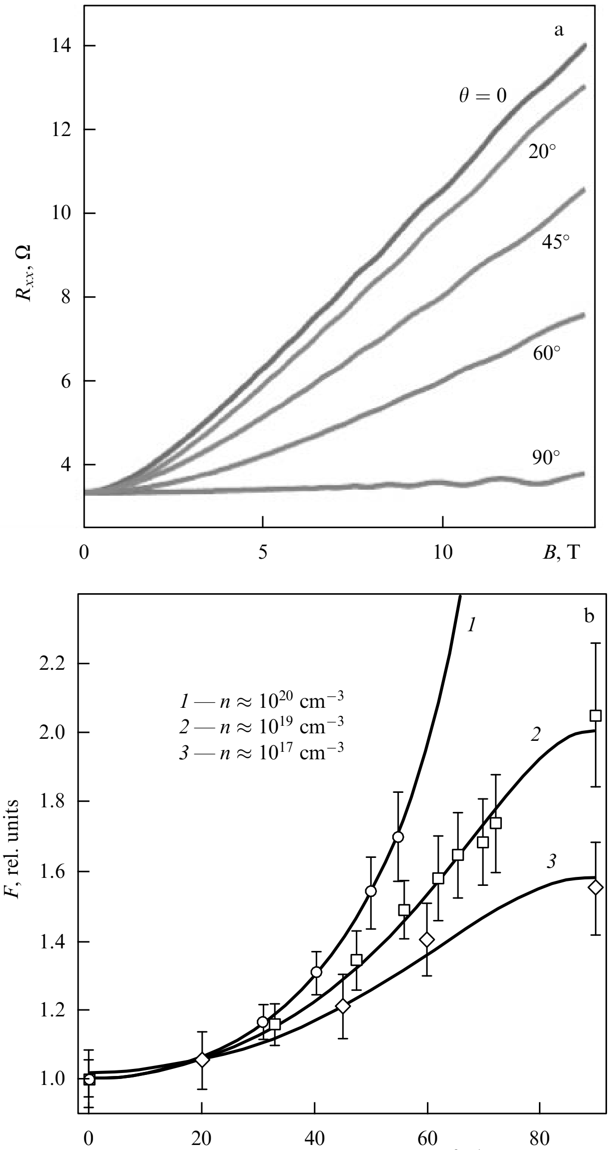

Figure 12. (a) Longitudinal resistance of a Bi_2Se_3 sample with $n \approx 10^{17}$ cm^{-3} versus the magnetic field, measured for different angles θ between the magnetic field direction and the sample axis c. (b) Angular dependences of SdH oscillation frequencies obtained using the Fourier analysis of oscillations for three samples with the indicated carrier concentrations. Solid curves show the experimental data fitting results using the models with a cylindrical ($n \approx 10^{20}$ cm^{-3}) Fermi surface (curve *1*) and with ellipsoidal ($n \approx 10^{17}$ and 10^{19} cm^{-3}) Fermi surfaces (curves *2* and *3*) [83].

compared with that in the sample with $n \approx 10^{20}$ cm^{-3} (Fig. 11b). As stated in [83], the Dirac surface state existed in the entire n variation range with the linear Dirac dispersion being preserved. But if the oscillations are associated with surface states, then their amplitude, obviously, should be constant for all concentrations, which was not observed.

Figure 12b shows angular dependences of the SdH oscillation frequencies for three samples with different concentrations, obtained using the Fourier analysis of oscillations. In samples with $n \approx 10^{17}$ cm^{-3} and $n \approx 10^{19}$ cm^{-3} (curves *3* and *2*), the oscillations were observed at angles θ up to 90°. According to [65, 67, 77–79], such SdH oscillation behavior should indicate the domination of 3D bulk transport in these samples. As the authors of [83] believe, the oscillation character corresponded to closed ellipsoidal Fermi surfaces (curves *2* and *3* in Fig. 12b). In the sample with $n \approx 10^{20}$ cm^{-3} (curve *1*), the oscillation amplitude decreased as θ was increased, and vanished at $\theta > 55°$. The angular dependence of the oscillation frequency for this sample can be well described as $F \propto 1/\cos\theta$. This, as well as the absence of oscillations at large θ, was taken in the papers cited above to be the proof of the observation of 2D oscillations associated with surface states in 3D TIs. In [83], this oscillation dependence is explained by the presence of an open cylindrical Fermi surface, although the results of previous studies of Bi_2Se_3 with large carrier concentrations [84] are different from the ones shown in Fig. 12b. Observation of SdH oscillations in a parallel magnetic field in the Bi_2Se_3 sample with $n \approx 10^{17}$ cm^{-3} contradicts the results of previous papers, because they indicated that in Bi_2Se_3 with a carrier concentration $n \sim 10^{17}$ cm^{-3}, the oscillations should have a 2D character.

It is interesting to discuss the results of the subsequent study of quantum oscillations in $Cu_xBi_2Se_3$ [85], which are radically different from the results of previous studies [82]. The authors studied the oscillation frequency dependence on the angle between the magnetic field and the single-crystal c axis using torque magnetometry, but in this case in magnetic fields up to 31 T. Unlike the oscillations in previous experiments, where they were observed in $Cu_{0.25}Bi_2Se_3$ and Bi_2Se_3 single crystals only at angles less than 35°, the oscillations were observed in [85] at angles up to 90°, that is, in the field parallel to the *ab* plane of the surface. The existence of oscillations in the angular range 0–90° usually indicates their connection with the 3D Fermi surface. Again, assuming a 3D ellipsoidal Fermi surface, the authors of [85] used the oscillation period to calculate the areas of Fermi surface cross sections and values of k_F^x, k_F^y, and k_F^z. These values were then used to find the bulk carrier concentration, which in six studied $Cu_xBi_2Se_3$ samples lay in the range $5.93 \times 10^{19} - 13.91 \times 10^{19}$ cm^{-3}. The angular dependence of the oscillation frequency $F(\theta)$ for low bulk concentration samples was well described by the expression $F(\theta) = F_0[\cos^2\theta + (k_F^x/k_F^z)^2 \sin^2\theta]^{-1/2}$, which corresponds to a closed ellipsoidal Fermi surface. Here, F_0 is the oscillation frequency at $\theta = 0$ (its value is a fitting parameter) and k_F^x/k_F^z is the ellipsoidal Fermi surface eccentricity. As the concentration increased, the Fermi surface increased in the z-direction. For the highest-concentration sample, the closed ellipsoidal Fermi surface model predicted the value $k_F^z = 4.69$ nm^{-1}, which exceeded the height of the Brillouin zone and therefore indicated the presence of an open 2D quasicylindrical Fermi surface.

Naturally, such a change in the dimensionality of the $Cu_xBi_2Se_3$ Fermi surface should be accompanied by a change in the oscillation character. For a high carrier concentration in the case of a quasi-two-dimensional Fermi surface, the experiment should show two frequencies of quantum oscillations: a high frequency associated with the thickened region of the Fermi surface and a low frequency associated with its 'neck' [85]. The higher frequency was observed in [83, 85], but the lower one had not been observed previously, which, as authors of [85] note, was confusing. In fact, the investigations in [82, 84, 85] repeat the work by Lahoud and coauthors [83], with the only difference that quantum oscillations were studied using another method.

Therefore, it follows from [82–85] that the observed angular dependence of quantum oscillations in $Cu_xBi_2Se_3$

samples in a magnetic field is associated not with a 2D surface state but with a 2D quasicylindrical Fermi surface. We note, however, that according to the results of both ARPES experiments [80] and quantum oscillation investigations [82], $Cu_xBi_2Se_3$ samples demonstrate Dirac dispersion, which is a characteristic feature of topological systems.

One of the main conclusions in [82–85] regarding the Bi_2Se_3 Fermi surface shape variation with the change in the bulk carrier concentration seems ambiguous, due to results of a recent paper [86], where 2D SdH oscillations of longitudinal ρ_{xx} and Hall ρ_{xy} resistances were observed in high-quality copper-doped Bi_2Se_3 single crystals with a high bulk carrier concentration and a 'metallic' dependence of the resistance on temperature. By rotating the investigated samples in a magnetic field, it was shown that they are 3D TIs with a series of parallel 2D conductive channels with the thickness $\approx 1-5$ nm, as it was in undoped Bi_2Se_3 [76].

Figures 13a, b show the longitudinal resistances of $Bi_{2-x}Cu_xSe_3$ with $n = 1.1 \times 10^{20}$ cm^{-3} and $n = 2.8 \times 10^{19}$ cm^{-3} as functions of the magnetic field, measured for different rotation angles θ at the respective temperatures 0.3 and 1.5 K. It is clear that as the perpendicular component of the magnetic field decreases due to the increase in the angle θ, the SdH oscillations begin at higher fields and their amplitude decreases. At $\theta > 30°$, $\rho_{xx}(B)$ oscillations were not observed. Although Fig. 13b shows only the upper parts of the $\rho_{xx}(B)$ curves, it is clear that the sample is superconducting. The inset in Fig. 13a shows the Hall resistance R_{xy} in the perpendicular ($\theta = 0$) magnetic field of 15–19.5 T. In can be seen that the function $R_{xy}(B)$ in high fields demonstrates a plateau instead of oscillations. Probably, as in the case of undoped Bi_2Se_3 [76], the authors observed the 'bulk quantum Hall effect' caused by transport through multiple 2D conducting channels in a 3D single crystal.

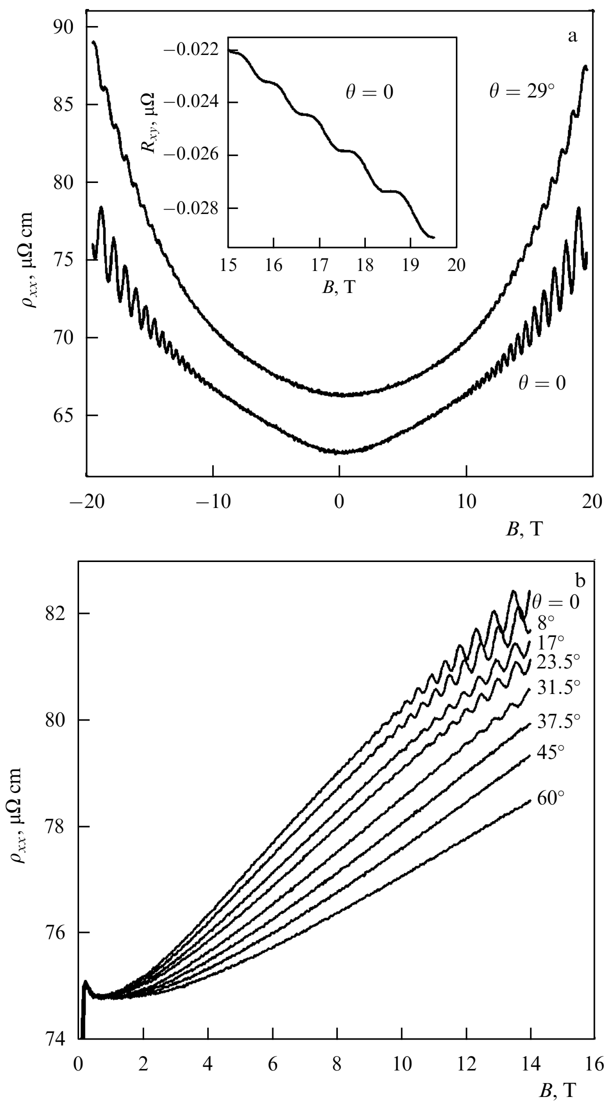

Figure 13. Longitudinal and Hall resistances of $Bi_{2-x}Cu_xSe_3$ single crystals with (a) $n = 1.1 \times 10^{20}$ cm^{-3} and (b) $n = 2.8 \times 10^{19}$ cm^{-3} versus the magnetic field. Measured for different tilt angles θ at respective temperatures of 0.3 and 1.5 K. The inset in Fig. a shows the Hall resistance R_{xy} in the field range 15–19.5 T in the perpendicular magnetic field [86].

The sample with $n = 2.8 \times 10^{19}$ cm^{-3} was of particular interest in [86]. Figure 14a shows $\Delta\rho_{xy}$ oscillation amplitudes as functions of the inverse magnetic field perpendicular component $1/B_{\perp} = 1/B\cos\theta$, measured for different angles θ in the field range 14.3–9.1 T. (In order to make the oscillation dependences on the magnetic field more visible, the authors used the quantity $\Delta\rho_{xy}$ obtained by subtracting a smooth baseline from the resistance ρ_{xy}.) The 2D character of these oscillations is obvious, because their amplitude decreases as θ is increased and becomes zero at $\theta > 31.5°$, while the positions of maxima on the curves depend only on the perpendicular component of the magnetic field $B_{\perp}$ and do not change as θ is varied.

Figure 14b shows the same $\Delta\rho_{xy}$ oscillations as in Fig. 14a, but in a wider field range 14.3–4.5 T. Curves clearly demonstrate oscillations with a large period, modulated by oscillations with a small period in higher fields (Fig. 14a). The amplitude of oscillations with a larger period barely changes with the angle θ, but their period and the positions of maxima (marked with arrows) depend on the sample tilt angle in the magnetic field, unlike small-period oscillations. This allows assuming that the large-period oscillations are associated with the Landau quantization of the 3D Fermi surface. Fourier analysis of the oscillations indicated the presence of two frequencies, F_b and F_s, corresponding to 3D and 2D contributions to the conductivity. At $\theta = 0$, $F_b = 39$ T and $F_s = 287$ T.

Figure 15 shows the results of the Fourier analysis of SdH oscillations $\Delta\rho_{xy}$, which illustrate the dependence of oscillation frequencies on the angle θ, shown in Fig. 14. It is clear that the bulk oscillation frequency F_b does not change with θ, which corresponds to weak anisotropy of the 3D Fermi surface in the plane of the θ variation. On the other hand, the frequency F_s changes with the θ variation and, as shown in the inset in Fig. 15, the values of F_s at different angles (dots) follow the dependence $\sim 1/\cos\theta$ (solid curve). This means that these oscillations depend only on the perpendicular component of the magnetic field $B_{\perp}$, and they are related to the Landau levels of the 2D Fermi surface.

The results in [86] showed that the topological insulator $Bi_{2-x}Cu_xSe_3$ with $n = 2.8 \times 10^{19}$ cm^{-3} supports SdH oscillations with two frequencies that correspond to both bulk and two-dimensional Fermi surfaces. If we recall the conclusions in [82–85] about the change in the Fermi surface shape in Bi_2Se_3 with the increase in the bulk carrier concentration and about the possible coexistence of closed ellipsoidal and open cylindrical Fermi surfaces, then it is reasonable to assume the existence of these Fermi surface shapes in one of the samples in [86], which is quite unlikely.

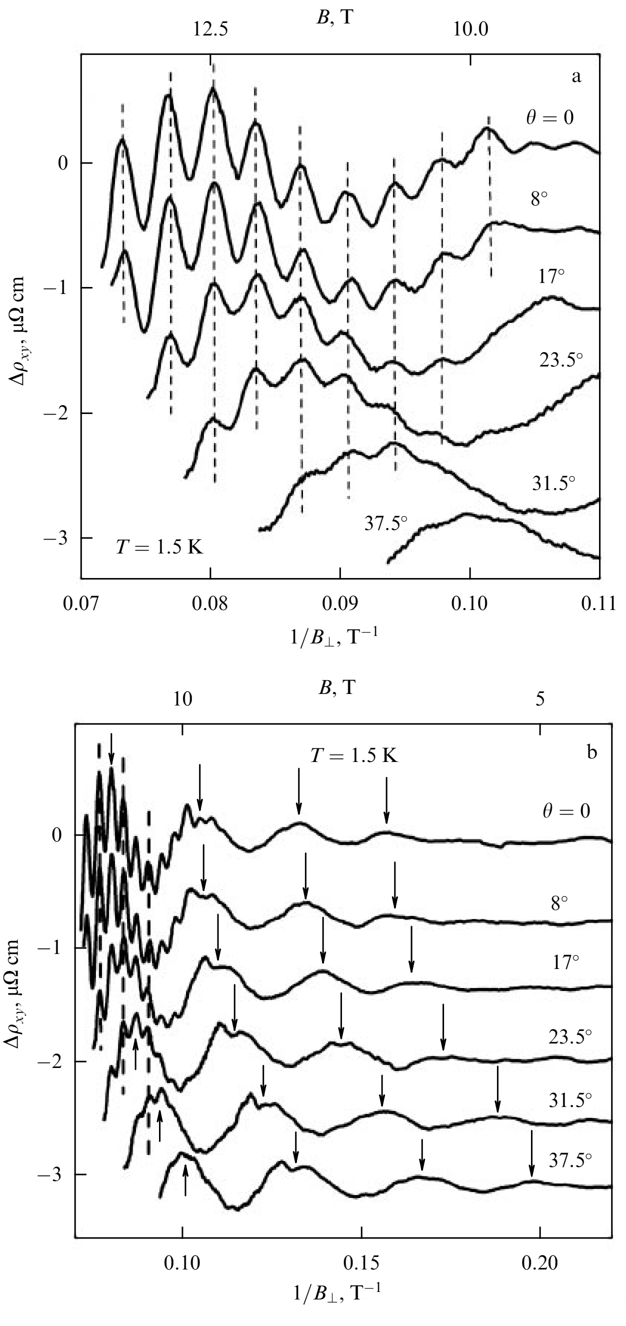

Figure 14. (a) $\Delta\rho_{xy}$ oscillations versus the inverse magnetic field perpendicular component $1/B_{\perp} = 1/B\cos\theta$, measured in a $Bi_{2-x}Cu_xSe_3$ sample with $n = 2.8 \times 10^{19}$ cm^{-3} for different tilt angles θ in the field range 14.3–9.1 T. Dashed lines indicate the positions of maxima. For visibility, the curves are shifted with respect to the curve for $\theta = 0$. (b) The same $\Delta\rho_{xy}$ oscillations as in Fig. a but in a broader field range: 14.3–4.5 T [86].

Using the SdH oscillation period allows finding the carrier concentration n_{2D} in a 2D layer from the Lifshitz–Onsager relation [60]. For 2D states, with the Landau level degeneracy taken into account [76], the concentration can be expressed as $n_{2D} = 2eF/h$. For example, in [86], measurements of the $Bi_{2-x}Cu_xSe_3$ sample with $n \approx 10^{19} - 10^{20}$ cm^{-3} resulted in the values $n_{2D} = 14 \times 10^{12} - 16 \times 10^{12}$ cm^{-2}. By comparing these values with the carrier concentration n in the bulk obtained from Hall measurements, we can calculate the effective thickness of the 2D layer $d_{2D} = n_{2D}/n$. The values specified above were used to calculate the 2D layer thicknesses, which was 4.9 nm for the sample with $n \approx 3 \times 10^{19}$ cm^{-3}, and this value is approximately

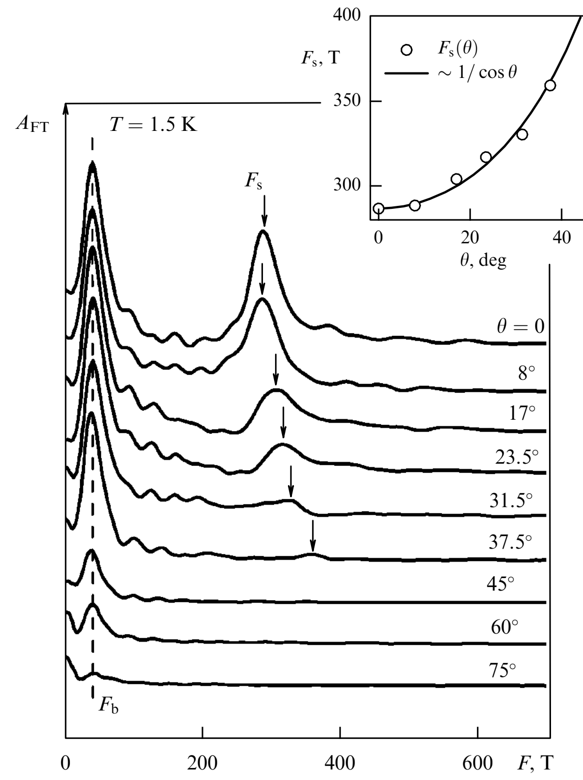

Figure 15. Results of the Fourier analysis of SdH oscillations in $\Delta\rho_{xy}$, which represent the oscillation frequency dependence on the angle θ ($Bi_{2-x}Cu_xSe_3$ sample with $n = 2.8 \times 10^{19}$ cm^{-3}, $T = 1.5$ K). A_{FT} is the Fourier transformation amplitude. The inset: dependences $F_s(\theta)$ (circles) and $\sim 1/\cos\theta$ (curve) [86].

the thickness of five 'quintuple layers' in the crystal structure, each being 1 nm thick [53]. At the same time, in the case of samples with a higher carrier concentration, $n \approx 1 \times 10^{20}$ cm^{-3}, the obtained thickness was $d_{2D} \approx 1.3$ nm, which approximately corresponded to a single quintuple layer.

Following the conventional procedure of the SdH oscillation analysis and using their temperature dependence (Fig. 16), the authors of [86] calculated the values of T_D, τ_D, the effective mobility μ_{eff}^{2D}, m_{eff}^{2D}, l_F, k_F, and v_F for a 2D surface layer. The specified parameters of a 2D system in the samples studied are shown in Table 1. The values of these parameters are very close to the ones obtained previously for the 2D surface conductivity in undoped and copper-doped Bi_2Se_3 samples [76, 82]. It is clear from Table 1 that, just as in [82], the values of v_F, τ_D, and l_F remain almost unchanged as the bulk carrier concentration increases by an order of magnitude as a result of doping with copper. This fact indicates that the copper doping does not affect the band structure of the initial Bi_2Se_3 material, and conduction electrons are located in the linear Dirac band.

When studying transport properties of Bi_2Se_3 epitaxial films with thicknesses $\approx 10-200$ nm in magnetic fields up to 14 T, Taskin and coauthors [87] observed 2D SdH oscillations with a frequency of 106.8 T, which were used to calculate the kinetic parameters of the system given in Table 1. The phase parameter was also calculated as $\beta = 0.4 \pm 0.04$, with the Berry phase equal to 0.8π. It is now easy to conclude that in single crystal Bi_2Se_3 3D TIs, both pure and copper-doped, as well as in thin Bi_2Se_3 films, the topological surfaces have very close fundamental kinetic parameters.

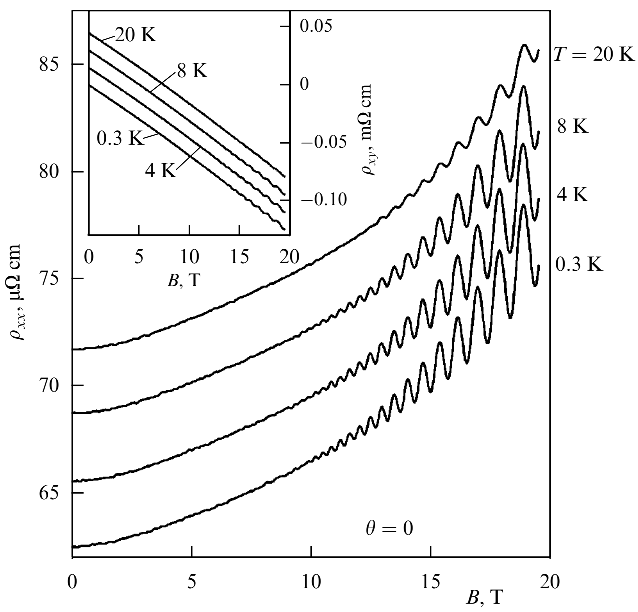

Figure 16. The ρ_{xx} resistance of a $Bi_{2-x}Cu_xSe_3$ sample with $n = 1.1 \times 10^{20}$ cm^{-3} in the magnetic field perpendicular to the sample surface at different temperatures. The inset shows the ρ_{xy} resistance under the same conditions. For visibility, all curves are shifted up with respect to the lower curve. It is clear that as the temperature increases, the oscillation amplitude significantly decreases [86].

Similar results were obtained when studying more complicated TI: Bi_2Te_2Se [71, 73, 88], $Bi_2Se_{2.1}Te_{0.9}$ [89], $Tl_{1-x}Bi_{1+x}Se_2$ [90], and $Bi_{2-x}Sn_xTe_2Se$ [91].

We first discuss papers [71, 88], where SdH oscillations were studied in Bi_2Te_2Se TIs. It was mentioned above that according to theory, 3D TIs should be insulators in the bulk, while Bi_2Te_3 and Bi_2Se_3 are semimetals. Usually, their Fermi level is located at the edge of the conduction band, and they demonstrate high conductivity. As a result, the bulk current in them always prevails over the surface current [62–65, 67, 69]. Ren and coauthors [71] found that with a slight Se surplus, Bi_2Te_2Se crystals can be obtained with a large bulk resistance and the Fermi level located inside the bulk band gap. In this hybrid material, the Se ions are located in the deepest 'sublayer' in each quintuple layer. Thus, $Bi_2Te_{1.95}Se_{1.05}$ samples with thicknesses up to 260 μm demonstrated clearly pronounced SdH oscillations associated with the surface state, which is confirmed by the data in Table 2. The experiments by Ren and collaborators were followed by paper [88], where quantum oscillations were studied in Bi_2Te_2Se samples with an even larger bulk resistance in magnetic fields up to 45 T. The obtained results, except for the 2D mobility value $\mu_{\rm eff}^{\rm 2D} = 3200 \pm 300$ cm^2 V^{-1} s^{-1}, turned out to be similar to the ones obtained earlier with the Bi_2Te_2Se sample [73]. The obtained large value of $\mu_{\rm eff}^{\rm 2D}$ was a strong argument supporting the assumption that the oscillations were associated with surface states.

Recently, in [89], 2D SdH oscillations were observed in p-type $Bi_2Se_{2.1}Te_{0.9}$ single crystals, despite a high carrier concentration in the bulk (2×10^{18} cm^{-3}) and the 'metallic' dependence of the resistance on the temperature. Results of a Fourier analysis of the oscillations showed a strong peak at the frequency $F \approx 23$ T with a sideband on the right-hand side of the peak, which was visible at low temperatures. As the temperature increased, this sideband disappeared. As the authors of [89] believe, this could indicate a small contribution of high-frequency oscillations, as was observed in other topological systems with complicated Fermi surfaces [62, 72]. As the angle θ of the sample tilt to the magnetic field increased, the oscillation amplitude rapidly decreased and vanished at large angles. The angular dependence of the oscillation maxima positions was in good agreement with the function $1/\cos\theta$, as it should be in the case of 2D quantum oscillations associated with topological surface states [63]. The oscillation frequency was used to calculate the values of $k_{\rm F}$ and the surface carrier concentration. The value of $k_{\rm F}$ turned out to be slightly smaller than the values of $k_{\rm F}$ obtained for other TIs, both p-type and n-type [63, 64, 71, 72], which indicates that the Fermi level is close to the Dirac point in the samples studied. Using the Lifshitz–Kosevich theory and the linear Dirac dispersion $v_{\rm F} = \hbar k_{\rm F}/m_{\rm eff}^{\rm 2D}$, the authors of [89] calculated the main kinetic parameters (see Table 2).

In [90], the SdH effect was investigated in two $Tl_{1-x}Bi_{1+x}Se_2$ single crystals with hole conductivity and the bulk carrier concentrations 3.4×10^{16} cm^{-3} and 1.7×10^{16} cm^{-3} in fields up to 9 T. The quantum oscillation amplitude dependences on the magnetic field component perpendicular to the sample surface were in good agreement with the expression $1/B_\perp = 1/B\cos\theta$. The oscillation frequency F was 209 ± 3 T. Assuming, in accordance with [92], the Fermi surface cross section to be round, the authors of [90] used the expressions $F = \hbar S_{\rm F}/(2\pi e)$, $S_{\rm F} = \pi k_{\rm F}^2$, and $S_{\rm F} = (2\pi^2)\, n_{\rm 2D}$ to calculate $k_{\rm F}$ and the surface carrier concentration $n_{\rm 2D}$, which turned out to be comparable with the ARPES data [93]. The values of $v_{\rm F}$, $T_{\rm D}$, $\tau_{\rm D}$, $\ell_{\rm 2D}$, $m_{\rm eff}^{\rm 2D}$, and $\mu_{\rm 2D}^{\rm SdH}$ were also obtained, and they are shown in Table 2.

Table 2. Parameters of 2D systems for samples from [71, 89–91].

Parameter \ Sample	Bi_2Te_2Se [71]	$Bi_2Se_{2.1}Te_{0.9}$ [89]	$Bi_{2-x}Sn_xTe_2Se$ [91]	$Tl_{1-x}Bi_{1+x}Se$ [90]
n, cm^{-3}	2.4×10^{17}	2×10^{18}	$\sim 10^{18}$	2.5×10^{16}
$F_{\rm s}$, T	64	23	—	209 ± 3
$n_{\rm 2D}$, cm^{-2}	1.5×10^{12}	5.8×10^{11}	2.8×10^{12}	5.1×10^{12}
$k_{\rm F}$, cm^{-1}	4.4	2.7	5.9	8.0
$m_{\rm eff}^{\rm 2D}/m_{\rm e}$	0.11	0.08	0.13	(0.03 ± 0.01)
$T_{\rm D}$, K	25.5	12	12.5	4.2
$\tau_{\rm D}$, s	4.8×10^{-14}	1.0×10^{-13}	—	2.9×10^{-13}
$\mu_{\rm eff}^{\rm 2D}$, cm^2 V^{-1} s^{-1}	760	2200	1300	2200
$v_{\rm F}$, m s^{-1}	4.6×10^5	3.9×10^5	4.6×10^5	4.1×10^5
$\ell_{\rm F}$, nm	22	39	—	120
γ	$(0.44 \pm 0.24)\,\pi$	π	$(0.8 \pm 0.2)\,\pi$	$(0.94 \pm 0.12)\,\pi$

The influence of Sn atom doping on the transport properties of $Bi_{2-x}Sn_xTe_2Se$ TI with $0 \leqslant x \leqslant 0.02$ was studied in [91]. The undoped n-type compound ($x = 0$) demonstrated a metallic temperature dependence of the resistance with the Fermi level located inside the conduction band. The introduction of Sn shifted this level inside the bulk band gap and for $x \geqslant 0.004$ the temperature dependence of resistance demonstrated a semiconducting character. The analysis of SdH oscillations directly proved that surface transport is dominant in massive Sn-doped Bi_2Te_2Se samples with a thickness of several micrometers (see Table 2).

In [91], besides the considered simple case, the authors observed a more complicated picture. For example, a Fourier analysis of the SdH oscillations in the sample with $x = 0.01$ indicated two frequencies: $F_1 = 70$ T and $F_2 = 132$ T, which corresponded to the respective wave vectors $k_F = 4.6 \times 10^6$ cm^{-1} and $k_F = 6.3 \times 10^6$ cm^{-1} and concentrations $n_{2D} = 1.7 \times 10^{12}$ cm^{-2} and $n_{2D} = 3.2 \times 10^{12}$ cm^{-2}. Due to the complicated character of these oscillations, the authors of [91] did not calculate the effective carrier masses or Dingle temperatures for every component.

Summarized data on the difference between the Fermi level energy E_F and the Dirac point energy E_D obtained over recent years from 2D SdH oscillations in 3D TIs [63, 64, 71, 72, 88, 90, 93] is shown in Fig. 17 [90]. As can be seen, there is only one case with the Fermi level located below the Dirac point, when the spins are carried by holes (the image also schematically shows the Dirac cone).

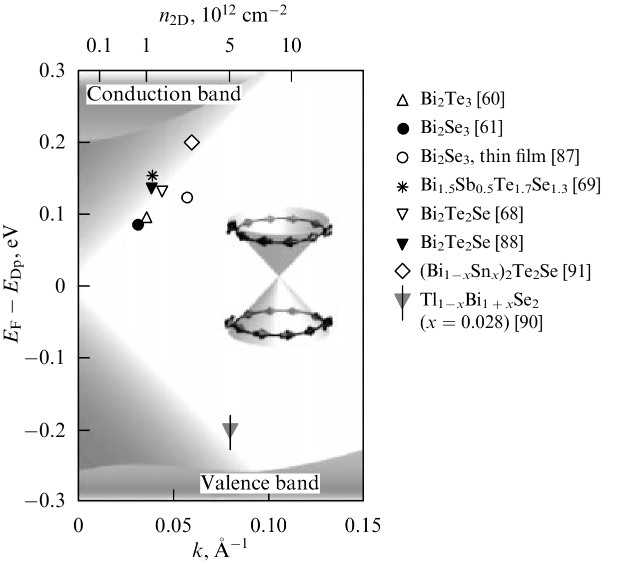

Figure 17. Differences between the Fermi level energy E_F and the Dirac point energy E_{Dp} determined from 2D SdH oscillations in the 3D TI indicated. The surface carrier concentration n_{2D} is plotted along the upper axis. The surface Dirac cone is schematically shown as well.

From the data presented above, it can be concluded that the ARPES experiments and magnetotransport experiments confirm the existence of 2D surface states in 3D TIs. However, until recently, the question regarding the value of the Berry phase in TIs remained open, because there was no reliable data on both the ARPES experiments and the transport experiments in the literature [63, 64], although the phase term in 2D SdH oscillations allows us to make sure once again that the observed oscillations are associated with Dirac fermions.

When both 2D and 3D carriers coexist in a sample, the index N of the field B_N in SdH oscillations plays a key role for the calculation of the Berry phase [1, 49]. However, the literature still does not give convincing answers to two questions. First, should B_N be chosen using the minima or the maxima of the SdH oscillation amplitude? And second, should the magnetoresistance or the magnetoconductance be used when calculating the Berry phase?

The importance of the N index definition in the phase analysis of SdH oscillations is clear from [71], where the Bi_2Te_2Se 3D-TI was studied. The authors of [71] defined the N indices using the ρ_{xx} resistance minima and obtained the value of the phase parameter $\beta = 0.22 \pm 0.12$ [see expression (3)]. Later, these results were processed again in [2] and the N indices were determined using the minima of the conductivity σ_{xx}. The same experimental data resulted in the value $\beta = 0.5$ and consequently the Berry phase $\gamma = \pi$, which corresponds to the SdH oscillation theory associated with Dirac fermions. This means that the approach developed in [63, 87] should be used in calculating the Berry phase. Obviously, the overlap of the Fermi level with the Landau level leads to a maximum in the electron density of states and hence to a conduction maximum. If the Fermi level is located between the Landau levels, where there are no electrons, then the density of states and conduction are minimal. In that case, some Landau levels below the Fermi level are filled and the next level is empty. This minimum in σ_{xx} can then correspond to a specific index N, while the maximum would correspond to the index $N + 1/2$.

Because the 2D and 3D conductivities are additive in a 3D TI, the measured resistances can be transformed into the conductivities $\sigma_{xx} = \rho_{xx}/(\rho_{xx}^2 + \rho_{xy}^2)$. Figure 18a shows the positions of σ_{xx} minima in the inverse magnetic field $1/B$ as a function of N (a fan diagram of Landau levels) for the sample with $n = 2.8 \times 10^{19}$ cm^{-3} [86]. The value of σ_{xx} shown in the upper part of the inset in Fig. 18a is calculated using the data from the resistance measurements (shown in Fig. 13b) at $\theta = 0$. Arrows indicate the indices N of the Landau levels. It is clear that the values N in Fig. 18a can be well fitted with the line with a fixed tangent, which also follows from the dependence of F/B_N on N, where $F = 287$ T is the result of the Fourier analysis of oscillations, shown in the lower inset in Fig. 18a. The dashed line in Fig. 18a intersects the N axis at the point 0.5. The conductivity of the TI oscillates in the magnetic field according to expression (3), which means that as $1/B \to 0$, the intersection of the straight line and the N axis give the phase parameter $\beta = \gamma/(2\pi)$ and the Berry phase $\gamma = \pi$. Figure 18b [86] shows fan diagrams of Landau levels in the sample with $n = 1.1 \times 10^{20}$ cm^{-3} for two tilt angles with respect to the magnetic field direction. The data correspond to the σ_{xx} minima. To verify the validity of the B_N choice according to [63, 88], the figure also shows the data that corresponds to the $N + 1/2$ maxima of the conductivity σ_{xx}. Straight lines (data extrapolation to $1/B \to 0$) intersect the x axis at the point $\beta = 0.45$, which leads to the phase $\gamma = 0.9\pi$. Similar data was obtained for the sample with $n = 1.2 \times 10^{20}$ cm^{-3} at the angles $\theta = 0, 22°, 36°$ [86]. Based on this, we can conclude that the Berry phase in the studied samples is $\gamma \approx \pi$ and does not depend on the direction of the magnetic field. The data on γ are shown in Table 1.

3. Conclusions

Currently, the study of TIs is the most rapidly developing field of solid state physics. A list of more than 30 TIs based on Bi, Sb, Se, Te, Tl, Sn, and Pb that were studied experimentally is

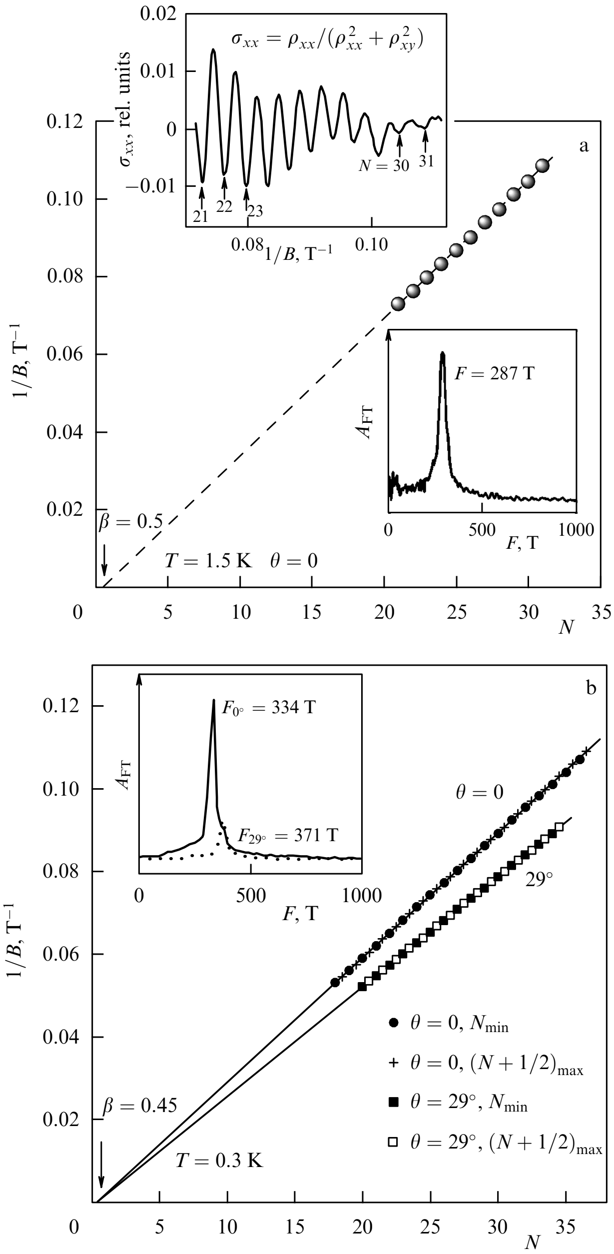

Figure 18. (a) σ_{xx} minima positions in the inverse magnetic field $1/B$ versus N (fan diagram of Landau levels) for a $Bi_{2-x}Cu_xSe_3$ sample with $n = 2.8 \times 10^{19}$ cm^{-3}. In the upper inset, the value of σ_{xx} calculated based on data presented in Fig. 13b at $\theta = 0$; arrows indicate the indexes N of the Landau levels. In the lower inset the Fourier analysis result. (b) Fan diagrams of Landau levels in the $Bi_{2-x}Cu_xSe_3$ sample with $n = 1.1 \times 10^{20}$ cm^{-3} for two tilt angles θ with respect to the magnetic field direction. The data corresponds to the σ_{xx} minima obtained from the experimental curves ρ_{xx}. The figure also shows data corresponding to $N + 1/2$ maxima of the conductivity σ_{xx}. The inset shows the results of the Fourier analysis [86].

given in [2], although there are many more materials that are topological insulators according to theoretical predictions, but have not been studied experimentally yet. Although the fundamental properties of TIs seem to be identified, the TI research field is at the early stage of development. Great effort will be needed to realize the unique possibilities of these interesting materials [8].

Not long ago, it was believed that TIs should be ideal insulators with the bulk carrier concentration $n \lesssim 10^{17}$ cm^{-3}, but it was shown recently that in 3D materials with high carrier concentration $n \sim 10^{19} - 10^{20}$ cm^{-3}, surface transport can dominate over the bulk transport at low temperatures. In the nearest future, researchers will hopefully discover new materials with larger band gaps, which would demonstrate TI properties at room temperature. As was shown in [91], a tin-doped Bi_2Te_2Se sample remains a TI even at the temperature of 100 K. An important task is also the growth of relatively pure material samples with the Fermi level located near the Dirac point of the surface state.

The quantum spin Hall effect allows the spin current to flow dissipationlessly and makes it possible to control the spin degrees of freedom with the electric field without the magnetic field. These properties can be used to create promising spintronic devices with low losses. The dependence of the electron spin on its momentum allows using these devices for memory storage in quantum computers, where the data cell unit will be the electron spin. Manipulations with spins are less energy consuming than charge variations in solid state storage devices. On the other hand, it is difficult to randomly change the electron spin in the surface layer of a TI, which prevents unwanted data loss [8].

Because superconductors have a band gap on the Fermi level, in some sense they turn out to be similar to insulators and can give rise to the fabrication of topological superconductors whose topological invariance is protected by the presence of a band gap [1, 94].

References

1. Qi X-L, Zhang S-C *Rev. Mod. Phys* **83** 1057 (2011)
2. Ando Y *J. Phys. Soc. Jpn.* **82** 102001 (2013)
3. Moore J E *Nature* **464** 194 (2010)
4. Zhang S-C *Physics* **1** 6 (2008)
5. v. Klitzing K, Dorda G, Pepper M *Phys. Rev. Lett.* **45** 494 (1980)
6. The Nobel Prize in Physics 1998, Press Release, 13 October 1998, http://www.nobelprize.org/nobel_prizes/physics/laureates/1998/press.html
7. Halperin B I *Phys. Rev. B* **25** 2185 (1982)
8. Hasan M Z, Kane C L *Rev. Mod. Phys.* **82** 3045 (2010)
9. Nagaosa N *Science* **318** 758 (2007)
10. König M et al. *Science* **318** 766 (2007)
11. von Klitzing K *Rev. Mod. Phys.* **58** 519 (1986); *Usp. Fiz. Nauk* **150** 107 (1986)
12. Krive I V, Rozhavskii A S *Phys. Usp.* **30** 370 (1987); *Usp. Fiz. Nauk* **152** 33 (1987)
13. Moore J E, Balents L *Phys. Rev. B* **75** 121306(R) (2007)
14. Haldane F D M *Phys. Rev. Lett.* **61** 2015 (1988)
15. Devyatov E V *Phys. Usp.* **50** 197 (2007); *Usp. Fiz. Nauk* **177** 207 (2007)
16. Bernevig B A, Hughes T L, Zhang S-C *Science* **314** 1757 (2006)
17. Wolf S A et al. *Science* **294** 1488 (2001)
18. D'yakonov M I, Perel' V I *JETP Lett.* **13** 467 (1971); *Pis'ma Zh. Eksp. Teor. Fiz.* **13** 657 (1971)
19. Murakami S, Nagaosa N, Zhang S-C *Science* **301** 1348 (2003)
20. Murakami S, Nagaosa N, Zhang S-C *Phys. Rev. Lett.* **93** 156804 (2004)
21. Zhang S-C, Hu J P *Science* **294** 823 (2001)
22. Sinova J et al. *Phys. Rev. Lett.* **92** 126603 (2004)
23. Castro Neto A H et al. *Rev. Mod. Phys.* **81** 109 (2009)
24. Kane C L, Mele E J *Phys. Rev. Lett.* **95** 226801 (2005)
25. Kane C L, Mele E J *Phys. Rev. Lett.* **95** 146802 (2005)
26. Wu C, Bernevig B A, Zhang S-C *Phys. Rev. Lett.* **96** 106401 (2006)
27. Bernevig B A, Hughes T L, Zhang S-C *Science* **314** 1757 (2006)
28. König M et al. *J. Phys. Soc. Jpn.* **77** 031007 (2008)
29. Gerchikov L G, Subashiev A V *Sov. Phys. Semicond.* **23** 1368 (1989); *Fiz. Tekh. Poluprovodn.* **23** 2210 (1989)
30. Fu L, Kane C L, Mele E J *Phys. Rev. Lett.* **98** 106803 (2007)
31. Roy R *Phys. Rev. B* **79** 195322 (2009)

32. Fu L, Kane C L *Phys. Rev. B* **76** 045302 (2007)
33. Kohmoto M, Halperin B I, Wu Y-S *Phys. Rev. B* **45** 13488 (1992)
34. Hsieh D Y et al. *Nature* **460** 1101 (2009)
35. Alpichshev Z et al. *Phys. Rev. Lett.* **104** 016401 (2010)
36. Teo J C Y, Fu L, Kane C L *Phys. Rev. B* **78** 045426 (2008)
37. Berry M V *Proc. R. Soc. Lond. A* **392** 45 (1984)
38. Wilczek F *Nature Phys.* **5** 614 (2009)
39. Bruëne C et al. *Nature Phys.* **8** 486 (2012)
40. Neupane M et al. *Phys. Rev. B* **85** 235406 (2012)
41. Bao L et al. *Sci. Rep.* **2** 726 (2012)
42. Zhang T et al. *Phys. Rev. Lett.* **103** 266803 (2009)
43. Reijnders A A et al. *Phys. Rev. B* **89** 075138 (2014)
44. Di Pietro P et al. *Phys. Rev. B* **86** 045439 (2012)
45. Akrap A et al. *Phys. Rev. B* **86** 235207 (2012)
46. Aguilar R V et al. *Phys. Rev. Lett.* **108** 087403 (2012)
47. Wu L et al. *Nature Phys.* **9** 410 (2013)
48. Hsieh D D et al. *Nature* **452** 970 (2008)
49. Hsieh D et al. *Science* **323** 919 (2009)
50. Nishide A et al. *Phys. Rev. B* **81** 041309(R) (2010)
51. Xia Y et al. *Nature Phys.* **5** 398 (2009)
52. Zhang H et al. *Nature Phys.* **5** 438 (2009)
53. Hsieh D et al. *Nature* **460** 1101 (2009)
54. Hong S S, Kundhikanjana W, Cha J J *Nano Lett.* **10** 3118 (2010)
55. Köhler H *Phys. Status Solidi B* **62** 57 (1974)
56. Golubkov M V et al. *JETP Lett.* **98** 475 (2013); *Pis'ma Zh. Eksp. Teor. Fiz.* **98** 533 (2013)
57. Pan Z-H et al. *Phys. Rev. Lett.* **106** 257004 (2011)
58. Fu L, Kane C L *Phys. Rev. Lett.* **100** 096407 (2008)
59. Qi X-L, Hughes T L, Zhang S-C *Phys. Rev. B* **78** 195424 (2008)
60. Shoenberg D *Magnetic Oscillations in Metals* (Cambridge: Cambridge Univ. Press, 1984); Translated into Russian: *Magnitnye Ostsillyatsii v Metallakh* (Moscow: Mir, 1986)
61. Zhang Y et al. *Nature* **438** 201 (2005)
62. Taskin A A, Ando Y *Phys. Rev. B* **80** 085303 (2009)
63. Qu D-X et al. *Science* **329** 821 (2010)
64. Analytis J G et al. *Nature Phys.* **6** 960 (2010)
65. Eto K et al. *Phys. Rev. B* **81** 195309 (2010)
66. Cao H et al. *Phys. Status Solidi RRL* **7** 133 (2013)
67. Butch N P et al. *Phys. Rev. B* **81** 241301(R) (2010)
68. Ren Z et al. *Phys. Rev. B* **84** 075316 (2011)
69. Checkelsky J G et al. *Phys. Rev. Lett.* **103** 246601 (2009)
70. Chen Y L et al. *Science* **325** 178 (2009)
71. Ren Z et al. *Phys. Rev. B* **82** 241306(R) (2010)
72. Taskin A A et al. *Phys. Rev. Lett.* **107** 016801 (2011)
73. Xiong J et al. *Physica E* **44** 917 (2012)
74. Kriener M et al. *Phys. Rev. Lett.* **106** 127004 (2011)
75. Mikitik G P, Sharlai Yu V *Phys. Rev. Lett.* **82** 2147 (1999)
76. Cao H et al. *Phys. Rev. Lett.* **108** 216803 (2012)
77. Köhler H, Fischer H *Phys. Status Solidi B* **69** 349 (1975)
78. Kulbachinskii V A et al. *Phys. Rev. B* **59** 15733 (1999)
79. Analytis J G et al. *Phys. Rev. B* **81** 205407 (2010)
80. Wray L A et al. *Nature Phys.* **6** 855 (2010)
81. Hor Y S et al. *Phys. Rev. Lett.* **104** 057001 (2010)
82. Lawson B J, Hor Y S, Li L *Phys. Rev. Lett.* **109** 226406 (2012)
83. Lahoud E et al. *Phys. Rev. B* **88** 195107 (2013)
84. Petrushevsky M et al. *Phys. Rev. B* **86** 045131 (2012)
85. Lawson B J et al. *Phys. Rev. B* **90** 195141 (2014)
86. Vedeneev S I et al. *JETP* **121** 65 (2015); *Zh. Eksp. Teor. Fiz.* **148** 75 (2015)
87. Taskin A A et al. *Phys. Rev. Lett.* **109** 066803 (2012)
88. Xiong J et al. *Phys. Rev. B* **86** 045314 (2012)
89. Shrestha K et al. *Phys. Rev. B* **90** 241111(R) (2014)
90. Eguchi G et al. *Phys. Rev. B* **90** 201307(R) (2014)
91. Ren Z et al. *Phys. Rev. B* **85** 155301 (2012)
92. Souma S et al. *Phys. Rev. Lett.* **106** 216803 (2011)
93. Kuroda K et al. *Phys. Rev. B* **91** 205306 (2015); arXiv:1308.5521
94. Tanaka Y et al. *J. Phys. Soc. Jpn.* **81** 011013 (2012)